The Spatial Structure and Interannual Variability of California Current System Transports

A Dissertation
Presented to
The Academic Faculty

By

Andrew Murphy Davis

In Partial Fulfillment
Of the Requirements for the Degree
Doctor of Philosophy in Earth and Atmospheric Science

Georgia Institute of Technology

August 2014

The Structure and Interannual Variability of California Current System Transports

Approved by:

Dr. Emanuele Di Lorenzo
School of Earth and Atmospheric Science
Georgia Institute of Technology

Dr. Taka Ito
School of Earth and Atmospheric Science
Georgia Institute of Technology

Dr. Annalisa Bracco
School of Earth and Atmospheric Science
Georgia Institute of Technology

Dr. Jean Lynch-Stieglitz
School of Earth and Atmospheric Science
Georgia Institute of Technology

Dr. Kevin Haas
School of Environmental Engineering
Georgia Institute of Technology

Date Approved: 4/24/2014

ACKNOWLEDGMENTS

This work could not have been completed without mentoring of my adviser and coauthor, Dr. Emanuele Di Lorenzo. Valuable assistance in the writing of chapter 5 was provided by Dr. Ali BelMadani, Dr. Niklas Schneider, Dr. Oleg Melnichenko, and Dr. Nikolai Maximenko. Dr. Bunmei Taguchi and Dr. Masami Nonaka also gave input while the work of chapter 4 was in its formative stages.

TABLE OF CONTENTS

LIST OF TABLES

LIST OF FIGURES

with an index of the stationary large-scale cross-shelf SSH gradient, as well as the v_e transport index for both integrations……25

Fig 11. (a) The projection of the first PC of CCS wind stress curl onto the full field. (b) comparison between this PC (PC1) and the wind stress curl gradient index. (c) the local mean wind stress curl..……,,,

LIST OF SYMBOLS AND ABBREVIATIONS

AR1- autoregressive order one

c_1- speed of the first-mode gravity wave

CALCOFI- California Cooperative Fisheries Investigations

CC- California Current

CCS- California Current System

CTW- Coastal Trapped Wave

EBC- Eastern Boundary Current

EKE- Eddy Kinetic Energy

ENSO- El Niño Southern Oscillation

EOF- Empirical Orthogonal Function

f_0- local coriolis parameter

H- effective depth

h_{curl}- sea surface height hindcast from wind stress

h_{coast}- sea surface height hindcast from coast

L_d- Rossby radius of deformation

NCC- Northern California Current

NCEP- National Center for Environmental Prediction

NEP- Northeast Pacific

OBC- OFES Boundary Condition

OFES- The Ocean Model for Earth Simulator

PC- Principal Component

PDF- Probability Density Function

PDO- Pacific Decadal Oscillation

r_e- radius of the earth

R- correlation coefficient

ROMS- Regional Ocean Modeling System

SCB- Southern California Bight

SCC- Southern California Current

SSH- Sea Surface Height

SSHa- Anomalous Sea Surface Height

u- zonal currents

v- meridional currents

v_a- anomalous meridional currents

v_{curl}- meridional currents hindcast from wind stress only

v_{coast}- meridional currents hindcast from coast only

v_e- anomalous alongshore currents

W- the Okubo-Weiss parameter

β- meridional gradient of f

Φ-Latitude

Φ_c- critical latitude for CTW energy

ζ- anomalous vorticity

η- anomalous sea surface height

τ- wind stress

ω- CTW frequency

ω_c- critical CTW frequency

SUMMARY

The California Current is the Eastern Boundary Current associated with the North Pacific Subtropical Gyre, transporting cold, nutrient-rich water equatorward. It is also an area of strong mesoscale eddy variance, as well as subsurface zonal currents known as striations. This work examines the causes and variability of these transports using a set of eddy-resolving ocean model simulations.

Large-scale meridional transports are found to be driven interannually by the dominant local pattern of wind stress curl variability. This contrasts with earlier work that suggested that these transports were forced principally by tropically-originating coastal-trapped waves.

While mesoscale eddies possess a large fraction of intrinsic variance, there is a deterministic component as well. North of the Southern California Bight this component is driven by the same pattern of wind forcing. To the south, eddies respond nonlinearly to both atmospheric and oceanic forcing.

Striations are found to develop in response to irregularities in the California coastline. They spin up along with the large-scale circulation, and their magnitude is constrained by the shelf.

Chapter 1: The Structure and Variability of the California Current System

The California Current System (CCS) comprises the Eastern Boundary Current (EBC) of the North Pacific Subtropical gyre. Like other EBC's, the CC is defined by a large offshore equatorward flow. It transports cold, nutrient-rich water from the pole towards the tropics, making it vital in meridional basin-scale heat exchanges and the Pacific climate system. The CC is also notable for seasonal productivity; coastal wind-driven Ekman upwelling drives drives extraordinarily strong primary production, peaking in summer (Hickey, 1998; Marchesiello et al., 2003). Like other EBCs, it is also a vital nutrient and temperature transport pathway for lower latitudes, making it an important component of the Pacific climate system (Gruber et al., 2006). Although the large-scale seasonal and upwelling dynamics of the CCS are well understood, the drivers of interannual modulation of the horizontal transports that comprise the California Current remain a subject of debate. Mesoscale (10-200km) activity is also particularly strong in the CCS. There are a number of standing eddies (meanders) offshore of notable topographic features (Centurioni et al. 2008), but seasonal eddy formation is also particularly robust (Strub and James, 2000; Chaigneau et al., 2009; Kurian et al., 2011).. These eddies also display a great deal of interannual variability- indicating that they may be driven externally as well as intrinsically variable (Stegmann and Schwing, 2007).

Recent observations have also shown a third possible method of CCS transport. Mean maps of global geostrophic zonal currents show bands of alternating east/west currents known as striations (Maximenko et al., 2005; 2008; Huang et al., 2007). These features persist in the mean such that they are considered semi-permanent, but there are indications that they vary in strength and position

interannually as well. Their signature is most apparent in the subsurface, but they may play a significant role in the overall horizontal mixing budget of the CCS. While it remains an open question as to the degree to which striations can affect the zonal transport of tracers, their prevalence in the global ocean makes them of general interest.

This work will examine the spatial structure and temporal variability of CCS currents, as comprising three basic components: large-scale meridional currents, mesoscale eddies, and striations. Its principal goal is to determine the sources of variability of these transports using the output of a high-resolution ocean model. While observations have determined the large-scale mean structure and seasonal variability of CCS transports (Hickey, 1998; Brink et al., 2000; Strub and James, 2000), they are not wholly satisfactory in a study on these spatial and temporal scales. Drifters, moorings, and ship-based observations possess neither the spatial resolution nor extent to capture a holistic picture of transports. And while AVISO satellite altimetry can provide the necessary detail in CCS surface currents, its observational record is too short to establish meaningful statistical relationships between transport variability and external forcing mechanisms on interannual scales. Realistic model hindcasts can provide these long-term records, as well as allow for sensitivity studies that can determine the necessary conditions for transport variance.

High-resolution regional oceanic circulation models generally offer greater temporal resolution and extent than most observations, but they have another relevant advantage over observations in establishing the drivers of oceanic variability. Ocean processes involve significant nonlinearity, both in the real ocean and in realistic, eddy resolving ocean models like those employed here. This results in unpredictability (i.e. intrinsic variability), adding uncertainty to any statistical

relationships drawn between oceanic variability and forcings without precise knowledge of the dynamics. In this work we employ an ensemble of hindcasts with identical atmospheric forcing. The variance shared between these integrations we can assume is deterministic and forced externally. The remaining component is intrinsic and unpredictable. Conclusions that are drawn from the ensemble as a whole as a whole will be more robust than those that apply only to a single member.

Results here suggest strongly that transport variance in the CCS is largely tied to local atmospheric modulations. The signature of local wind stress is present both in the large-scale alongshore currents, and in eddies north of the Southern California Bight. This contrasts with hypotheses that CCS transports are dominated by forcing related to basin-scale climate phenomena (Clarke and Dottori, 2008; Dottori and Clarke, 2009), and portrays the region as more local and self-contained.

Among other effects, this places a larger burden on climate modelers, as an effective capture of tropical or basin-scale North Pacific dynamics will not necessarily imply capture of CCS transports. Characterization of transport variance and its effect on ecosystems and tracer distribution will hinge on an ability to capture local wind patterns.

Our work on the forcing mechanisms of North Pacific striations reaches a complementary conclusion: striations are a phenomenon wholly distinct from mesoscale eddies, resulting from instabilities within the CC. This means that they are also ultimately wind-driven. While the sensitivity analysis employed here is incapable of hindcasting the variability of these striations, their structure is also determined by topography and atmospheric patterns.

Chapter 2: The ROMS model and its application to long-term CCS variance

This work makes extensive use of the output of the Regional Ocean Modeling System (ROMS). ROMS is an eddy-permitting ocean model that solves the incompressible primitive equations. It employs terrain-following coordinates, which allow for more accurate bottom topography effects in coastal environments (Schepetkin and McWilliams, 2003; Haidvogel et al., 2008). ROMS has an extensive publication history, and has been used to successfully model both the mean CCS and its variability on multiple spatial and temporal scales.

Part 3 (examining the variability of large-scale alogshore transports) and Part 4 (examining the interannual variability of mesoscale eddies) employ three Northeast Pacific regional ROMS model hindcasts from 1958-2008 on a 10 km grid. At the surface are prescribed fluxes of momentum and heat derived from NCEP Reanalysis II (Kalnay, 1996), corrected to avoid long-term drifts in the surface temperatures and salinity as in Di Lorenzo et al. (2009). The model domain has three open ocean boundaries with a radiation boundary condition (Marchesiello et al., 2001) to allow disturbances to propagate out of the model computational domain. Also included is a nudging to time-dependent changes at the open boundary derived from the long-term hindcast of the Ocean Model of the Earth Simulator (OFES)- a global eddy-resolving model with 10km average resolution (Masumoto et al., 2004). The two ROMS integrations employing this OFES boundary condition are denoted “OBC.” “OBC2” was initialized with the final month of “OBC1”, but subsequently forced identically, giving it a differing initial condition. The OFES hindcast also uses NCEP surface fluxes, making it consistent with our nested ROMS computations (Figure 1).

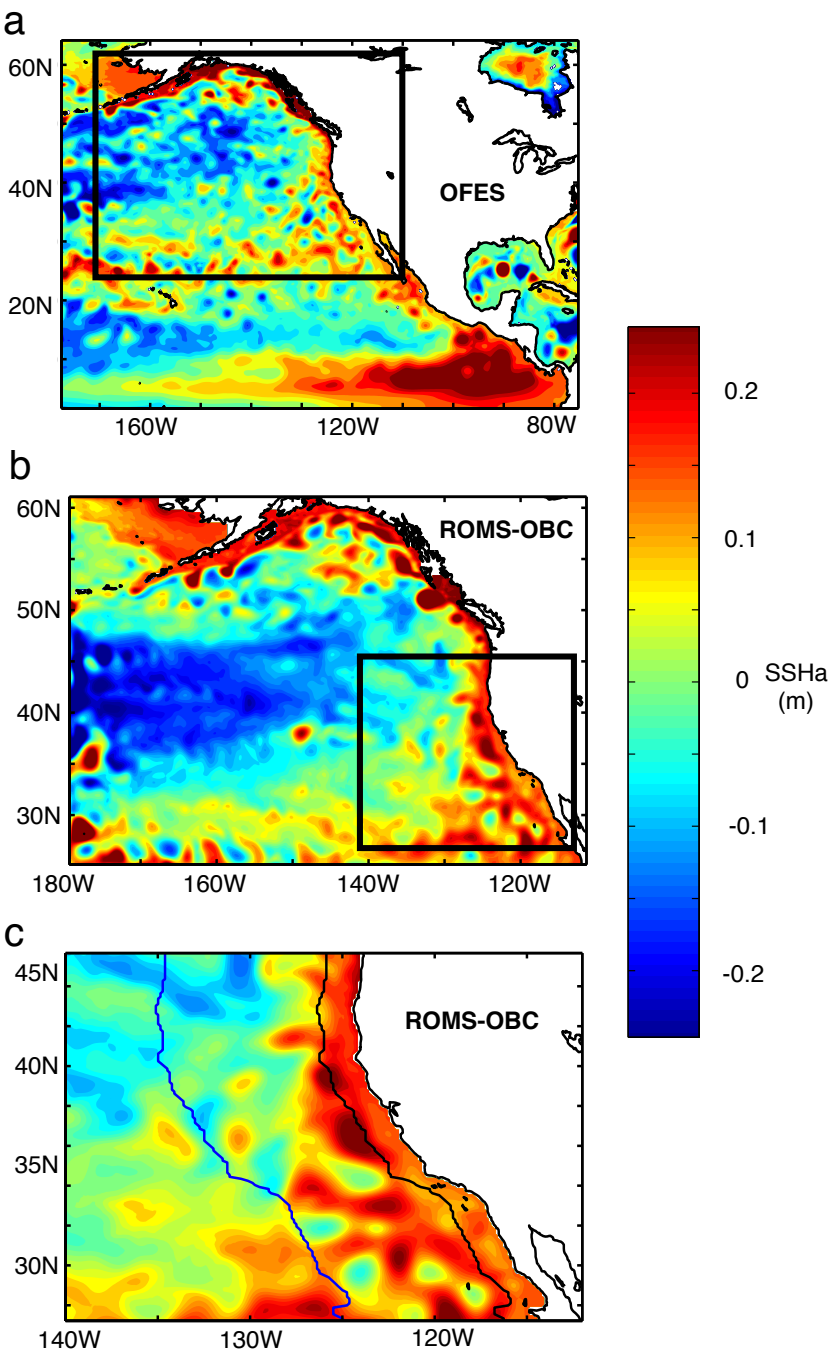

Figure 1 - (a) SSHa from the February 1998 ENSO event from the global ocean model OFES, with a black rectangle marking the computational domain of our ROMS integrations. (b) February 1998 SSHa derived from the output of our ROMS integration employing the OFES boundary condition (OBC), with a black rectangle marking the CCS region. (c) This region in more detail, with CC boundaries given by the black and blue lines.

This nudging at the southern boundary of the integration allows for the introduction of signals from outside the computational domain communicated through coastal-trapped waves (CTW's). Our principal interest is in any possible influence from the El Nino Southern Oscillation (ENSO) on the CCS. As the leading mode of Pacific basin-scale oceanic variability, ENSO influence must be included in order to test the effectiveness of tropical dynamics in forcing the CC (Figure 2A,B).

As a control, we employ a third ROMS integration, denoted "no OBC," which excludes this OFES nudging and incorporates a purely climatological southern boundary condition. While this integration has no influence from tropical CTW's, it does still carry an ENSO signal communicated through the atmospheric bridge in its NCEP forcing (Figure 2C). By comparing this "no OBC" integration to "OBC 1" and "OBC 2," we can determine the respective contributions of local and tropical ENSO forcing to CCS variability. The details of the three hindcasts are given in Table 1.

Table 1 – ROMS integrations used diagnosing large-scale meridional transport and mesoscale eddy variability

Name	Resolution	Forcing	Boundary Condition	Initialization
OBC1	10km w/ 30 vertical levels	NCEP Reanalysis II	Radiative w/ nudging to OFES	after spin-up from rest
OBC2	10km w/ 30 vertical levels	NCEP Reanalysis II	Radiative w/ nudging to OFES	with final record of OBC1
no OBC	10km w/ 30 vertical levels	NCEP Reanalysis II	Radiative w/ climatology	after spin-up from rest

This hindcast ensemble approach also allows for the separation of variance into a component that is forced (deterministic), and an intrinsic (random) fraction. By computing correlations between the same variable across integrations, we can quantify these respective fractions explicitly (i.e. common, shared variance should be forced, either by the shared NCEP winds or by the OFES boundary condition). This

approach will be vital in section 4, largely because mesoscale eddy formation is such an intrinsically variable process. Large-scale currents are significantly more deterministic, so we restrict the analysis in section 3 to “OBC 1” and “no OBC.”

A number of more specialized ROMS integrations were used in order to study the formation of striations and their sensistivity to topography in section 5. These runs are described in detail in section 5.1.

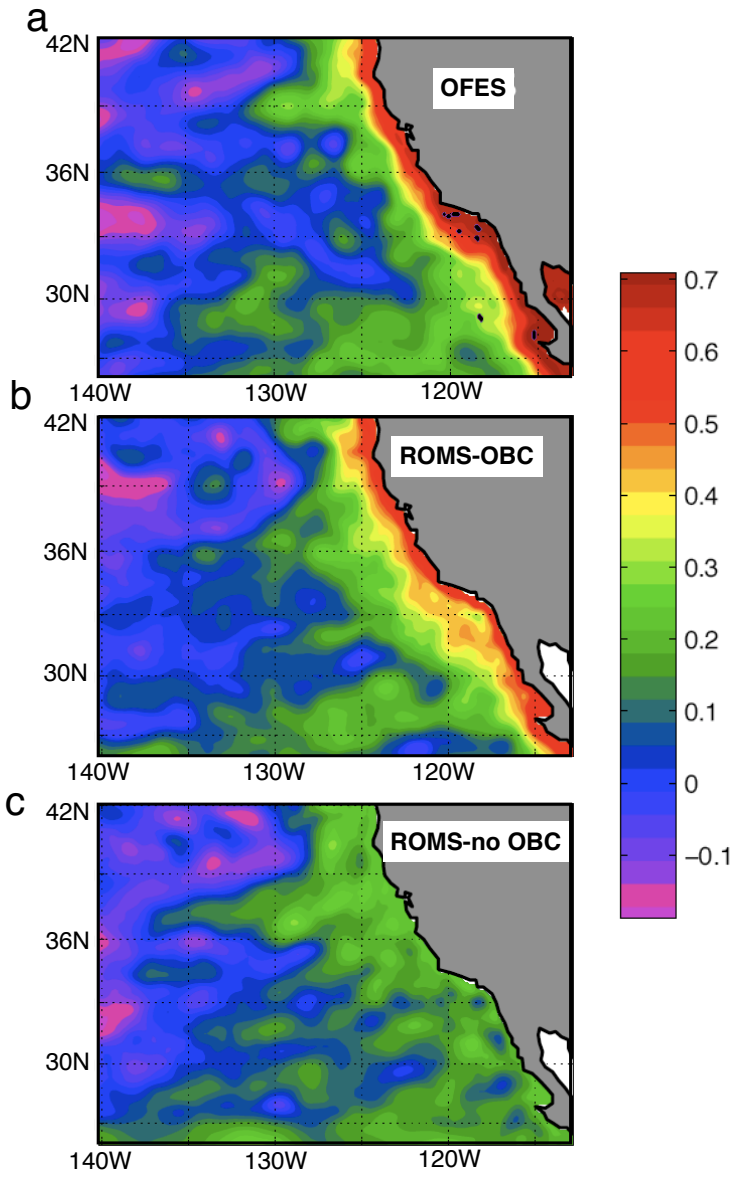

Figure 2 - (a) Correlations between Nino 3.4 and OFES SSH record, (b) SSHa from our ROMS integration using OFES boundary conditions (OBC), and (c) a ROMS integration forced only by climatology (no OBC). ROMS captures the equatorial signal, but with some damping, with a maximum correlation of 0.6 rather than 0.7 in OFES.

Chapter 3: Interannual forcing of large-scale meridional CCS transports

3.1: Local and remote forcing of alongshore currents

In this section, we examine the interannual modulation of large-scale alongshore CCS transports. It has been suggested (Clarke and Dottori, 2008) that, in the CCS, interannual variability of sea surface height (SSH) and meridional velocity (v) is primarily forced remotely, by an equatorial SSH signal propagating first poleward along the coast as a coastally trapped wave (CTW) and then offshore as a long Rossby wave (Figure 3A). This mechanism would also give rise to temperature, subsurface salinity (Dottori and Clarke, 2009), and plankton anomalies (Clarke and Dottori, 2008). The SSH signal would then generate geostrophic alongshore currents and tilt isopycnals, causing horizontal and vertical advection. If this mechanism did, in fact, dominate, it would imply a greater role for ENSO and other low-latitude phenomena in determining the physical and biological variability of the CCS. If the CCS were forced primarily by local wind anomalies, it would instead suggest that the CCS is a more closed, self-contained system. The principal aim of this section is to determine whether equatorial signals entering the domain through CTW's (remote forcing) or local atmospheric variability (local forcing) dominates interannual variability of surface meridional currents.

The CCS region is strongly stratified and has a narrow continental shelf, making it particularly conducive to the generation and propagation of CTW's. These waves have been detected by in situ measurement (Mooers and Smith, 1968) for over forty years, and have also been established to be a driver of alongshore shelf currents (Hickey, 1984). They propagate at speeds between 40 and 90 cm/s (Enfield

and Allen, 1980) and transmit coastal sea level and cross-shelf velocity signals poleward. Equatorially originating CTW's are a strong source of interannual variability that has been associated with ENSO (Hickey,1984; Pares-Sierra and O'Brien, 1989). Although CTW's can be generated within the CCS region by wind stress curl anomalies or riverine input (Gill, 1982), our primary interest is in low-frequency CTW's of equatorial origin.

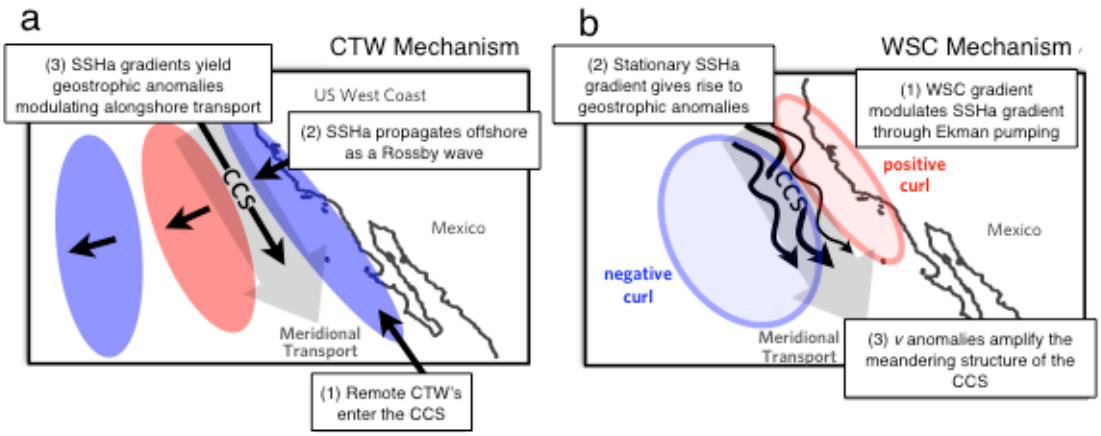

Figure 3 - Conceptual diagrams of the (a) coastal-trapped wave (CTW) and the (b) wind stress curl (WSC) mechanisms of CCS alongshore current (*v*) variability.

While it has been established (Enfield and Allen, 1980; Enfield and Allen, 1983; Chelton and Davis, 1982; Battisti and Hickey, 1984) by in situ measurement (largely tide gauges) that equatorially generated CTW's play a major role in the low-frequency fluctuations in SSH of the Eastern Pacific coast (within 100-200km of shore), it remains an open question as to whether they strongly influence variability in SSH and currents further offshore (> 200 km) in EBC regions.

CTW amplitude decreases exponentially away from a coastline, but the associated signal can travel offshore by means of a Rossby wave. For a wave of

specific frequency, there exists a critical latitude Φ_c. At latitudes where the value of $\Phi < \Phi_c$, the response to an SSH anomaly is that of a CTW, whereas where $\Phi > \Phi_c$, energy propagates westward as a low-frequency Rossby wave (Schopf 1981, Cane & Moore 1981). The critical frequency for Rossby wave propagation from a purely meridional boundary at latitude Φ has been determined to be

$$\omega_c = \frac{c_1}{2\tan(\phi) r_e} \quad (1)$$

where c_1 is the phase speed of the first-mode gravity wave, and r_e is the radius of the earth. Critical frequency will decrease both with increasing latitude and with any deviations from a strictly meridional coastline (due to a reduced beta effect) (Fu and Qiu, 2002). Clarke and Shi (1991) calculated this critical frequency for all of the world's major coastlines. In the CCS region, these frequencies are all on the order of around one year. Because of bottom frictional effects, as well as energy leaking as Rossby waves, CTW's will be necessarily damped as they propagate (Dorr and Grimshaw, 1986). This effect should be amplified by the geometric irregularity of the California coastline (Grimshaw and Allen, 1988). For this reason, the variance explained by coastally-originating Rossby waves can be expected to decrease poleward.

While remote forcing is transmitted by CTW's, on yearly time scales local forcing is dominated by wind stress anomalies and associated Ekman pumping (Hickey, 1998). The resulting SSH and v anomalies propagate westward as Rossby waves.

Our initial question is whether low-frequency variability of meridional currents in the CCS are due to the influence of local wind stress or remote CTW-generated Rossby waves. Observations of SSH from the TOPEX/Poseidon satellite have shown that the influence of coastally generated slow Rossby waves in the Northern Pacific is limited to a region 3000—4000 km offshore. Local wind-driven waves (reconstructed from climatological data) account for nearly all of the variance in the central North Pacific, but have less influence in nearshore (< 1000 km offshore) regions like the CCS (Fu and Qiu,2002).

Recent analysis of coastal northeast Pacific ROMS hindcasts has found that while CTW's excited by equatorial sea surface height anomalies did penetrate as far as the Gulf of Alaska, variability was largely accounted for by local rather than remote forcing (Hermann et al., 2009; Masson and Fine, 2012).

Using SSH, zonal and meridional surface velocities u and v, temperature and salinity data from California Cooperative Oceanic Fisheries Investigations (CalCOFI) Dottori and Clarke (2009) concluded that dynamic height anomalies (and the associated horizontal currents and vertical motion of the thermocline) in the CCS are dominated by long Rossby waves, particularly those excited equatorially by CTW's (Figure 3A). The spatial and temporal aliasing of the CalCOFI sampling grid may allow reasonable resolution of the SSHa transients associated with CTW/Rossby waves ~100-200km but does not resolve the effects of the meandering currents that are characterized by finer scale structure (< 200km).

We propose a revised wind stress curl mechanism (Figure 3B) dominating the low-frequency modulation of CCS meridional transport. Through Ekman pumping, wind stress curl alters the background stationary SSH gradient and generating geostrophic anomalies.

In a shallow-water quasi-geostrophic framework, wind stress is the primary driver of vorticity.

$$\frac{D(\zeta + \beta y + \frac{f_0}{H}\eta)}{Dt} = curl(\tau) \tag{2}$$

With a standard streamfunction, this can be linearized to yield

$$\frac{\partial \nabla^2 \psi}{\partial t} + \beta \psi_x - \frac{1}{L_d^2}\frac{\partial \psi}{\partial t} = curl(\tau) \ . \tag{3}$$

where L_d represents the Rossby radius of deformation. An assumption of large spatial scales leads us to neglect relative vorticity and beta terms. Differentiating in x leaves that

. $$\frac{\partial v}{\partial t} = L_d^2 \frac{\partial (curl(\tau))}{\partial x} \tag{4}$$

We propose that these dynamics govern the large-scale variability of CCS meridional transports and energize the regional scale meandering jets.

Our approach is to hindcast the spatial and temporal evolution of SSHa and anomalous meridional currents (v_a) over the period 1950-2008 using an eddy-resolving ocean model with two configurations that respectively include and exclude the effect of CTW's of equatorial origin. Using this model output we quantify how much of the total variance of SSHa and v_a in the CCS region can be explained by

CTW's and by local wind forcing. From this analysis it can be determined where and by what margin local and remote forcing dominate the low-frequency variability of the equatorward meridional flow in California Current.

Here we make no attempt to address the relative contributions of wind stress curl and CTW dynamics to shelf variability. While event-scale tropical CTW's can have a dramatic effect on the California coastal shelf, neither models nor AVISO satellite observations can properly resolve fine-scale coastal variance, and it is not considered here. Event-scale CTW's are also outside the scope of this study, as its primary question is the degree to which remote forcing influences interannual transport variability

3.2 Observed Rossby wave propagation

Variance associated with shorter, nonlinear Rossby waves (eddies) will be addressed in chapter 4, so mesoscale (10km-200km) variability was removed by applying a 200 km spatial running mean to individual SSHa records. Not only does this spatial filtering remove variability associated with eddies, but it also restricts our analysis to large-scale (>200km) Rossby waves on the order of those generated by CTW's.

To determine the phase speed of the long waves as measured by our model, we computed correlations between the SSHa time series at the coast and SSHa at all points west for lags up to 48 months for several lines of latitude- 29.1° N, 33.5° N, 37.8° N, and 41.9° N. (Figure 4). Wave speeds calculated with this method are on the order of cm/s and decrease with higher latitude. Using these data we arrived upon an approximate set of phase speeds linearly dependent on latitude, which we used to

construct SSHa and alongshore velocities in eq. 5 through 9 (Section 3.4). Measured speeds went from 3.9 cm/s at 29° N (consistent with the Dottori and Clarke (2008) estimate at the latitudes of the southern CCS) to 1.9 cm/s at 42° N.

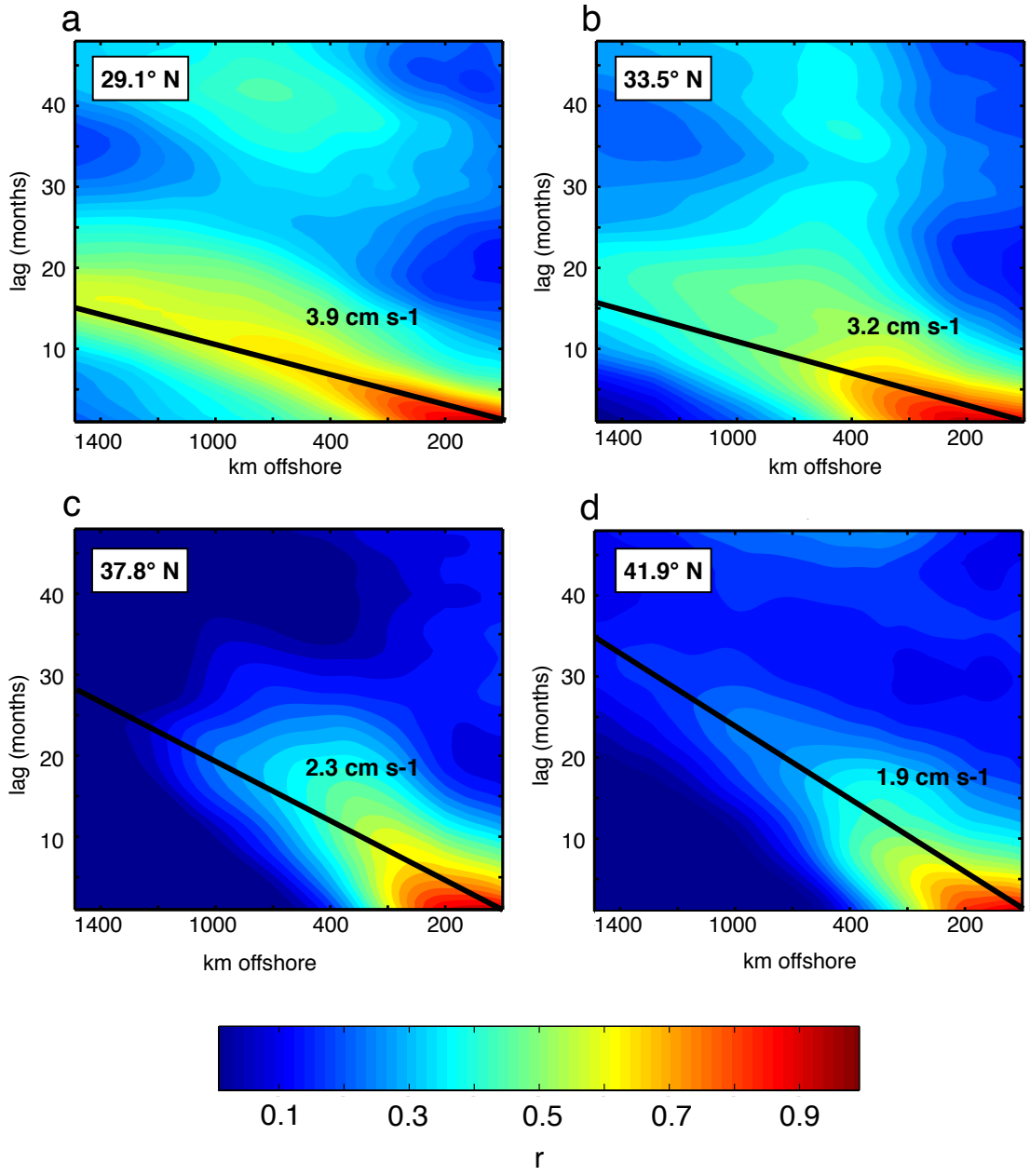

Figure 4 - Correlations between coastal SSHa and spatially filtered offshore SSHa for lags of up to four years by month for latitudes (a) 29.1° N, (b) 33.5° N, (c) 37.8° N, and (d) 41.9° N. The black line indicates maximum correlation and thus wave speed. Long Rossby wave speed decreases with latitude.

3.3 Offshore propagation of tropical/coastal signals

In order to determine the amount of variance in SSHa associated with remote CTW forcing, we computed pointwise correlations with Niño 3.4 for lags of 0, 6, 12, and 18 months (Figure 5A—D). The ENSO signal propagates offshore as it weakens, in agreement with theory. Corresponding maps correlating v_a and Niño 3.4 (Figure 5E—H) show only a narrow coastal band of tropical influence which disappears at with time. A third set correlating v_a and the first time derivative of Niño 3.4 (Figure 5I—L) (as in Dottori and Clarke's (2008) hypothesis) also shows little evidence of a remote signal.

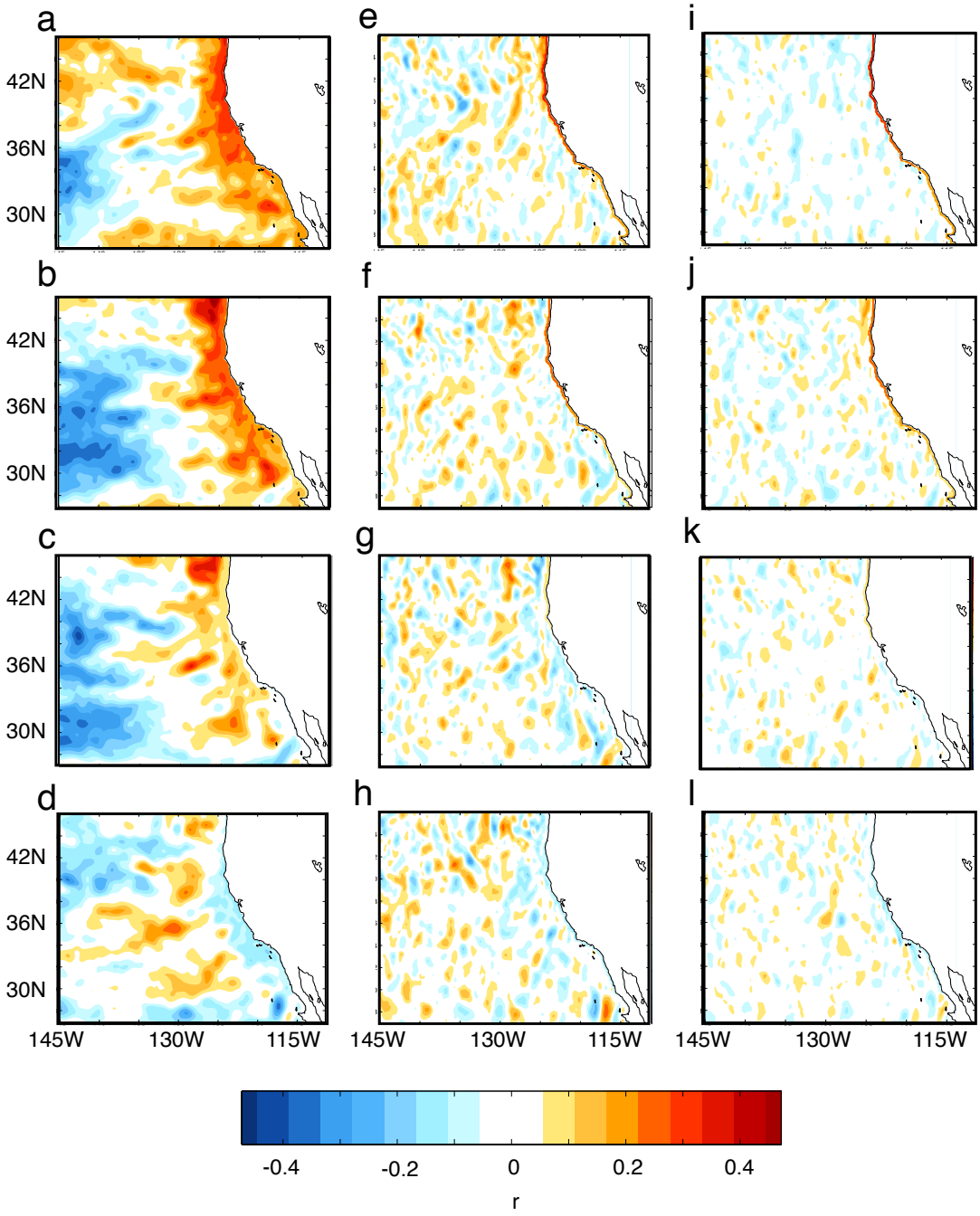

Figure 5 - Lagged pointwise correlations with Niño3.4 at 0, 6, 12, and 18 months for (a-d) SSHa and (e-h) geostrophic v_a . (i-l) Corresponding correlations between geostrophic v_a and the first time derivative of Niño3.4.

To further study the influence of Rossby waves on SSHa and v_a, we introduce a coordinate system with the y-axis normalized to the coastline (Figure 6A,B). We also introduce a rotated, alongshore current v_e (Figure 6C,D). Although it captures local flow better than a purely meridional velocity, this analysis is largely insensitive to the rotation.

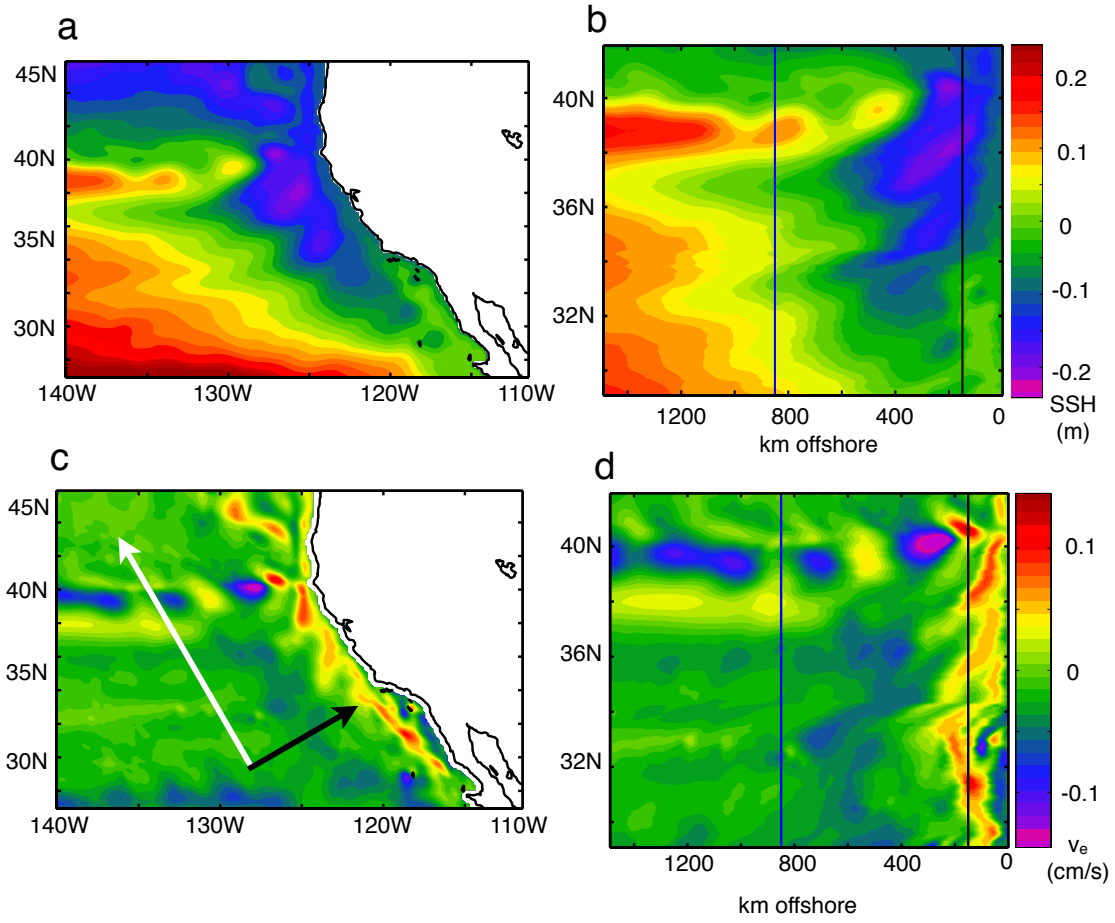

Figure 6 - (a) Mean SSH from our ROMS integration employing the OFES boundary condition, and (b) the same record in our coordinate system normalized to the coast. (c) The corresponding mean for our alongshore meridional velocity v_e (The white vector points in the direction of positive v_e). (d) The same field in the normalized coordinate system.

To determine the fraction of variance explained by the offshore propagation of the coastal signal we computed maps of the maximum correlation between each

point offshore and the coast for lags up to 3 years, as well as maps of the month in which this maximum correlation was found. These are given for the full field, the large-scale component, and the mesoscale component for both SSHa (Figure 7) and v_e (Figure 8). While there is little offshore propagation in the mesoscale, large-scale SSHa shows a strong pattern of correlation decreasing offshore (Figure 7B), as well as robust, linearly increasing time lags (Figure 7D), indicating that Rossby waves play a dominant role in offshore, large-scale SSHa variance.

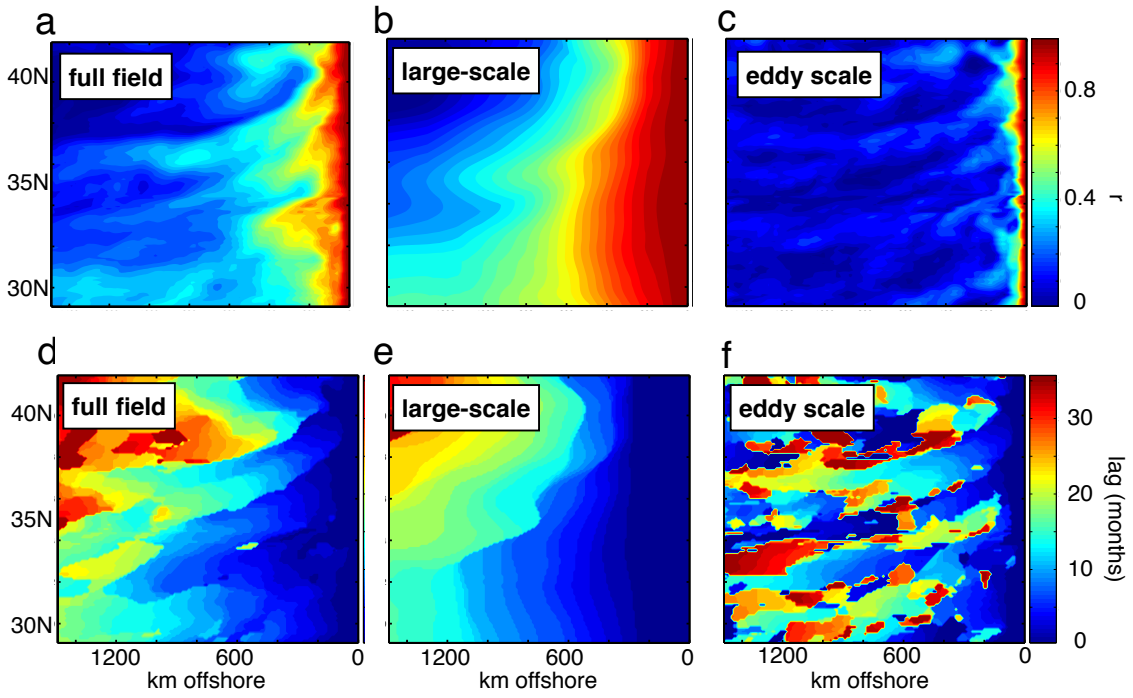

Figure 7 - (a) Maximum correlations over lags of up to three years between offshore and coastal SSHa using the full SSHa field, (b) the spatial-lowpassed field, and (c) the highpassed field. (d), (e), and (f) The the corresponding lags, in months, for which this maximum correlation is found.

In contrast, large-scale v_e shows strong correlations only in the nearshore (Figure 8B). The lag at which this correlation occurs is 0 months (Figure 8D),

indicating that this is a feature of the spatial smoothing, rather than Rossby waves. This would suggest that v_e variance does not propagate offshore from the coast effectively, in contrast to the CTW hypothesis. The same analysis performed on the mesoscale SSHa and v_e shows no sign of coherent offshore propagation.

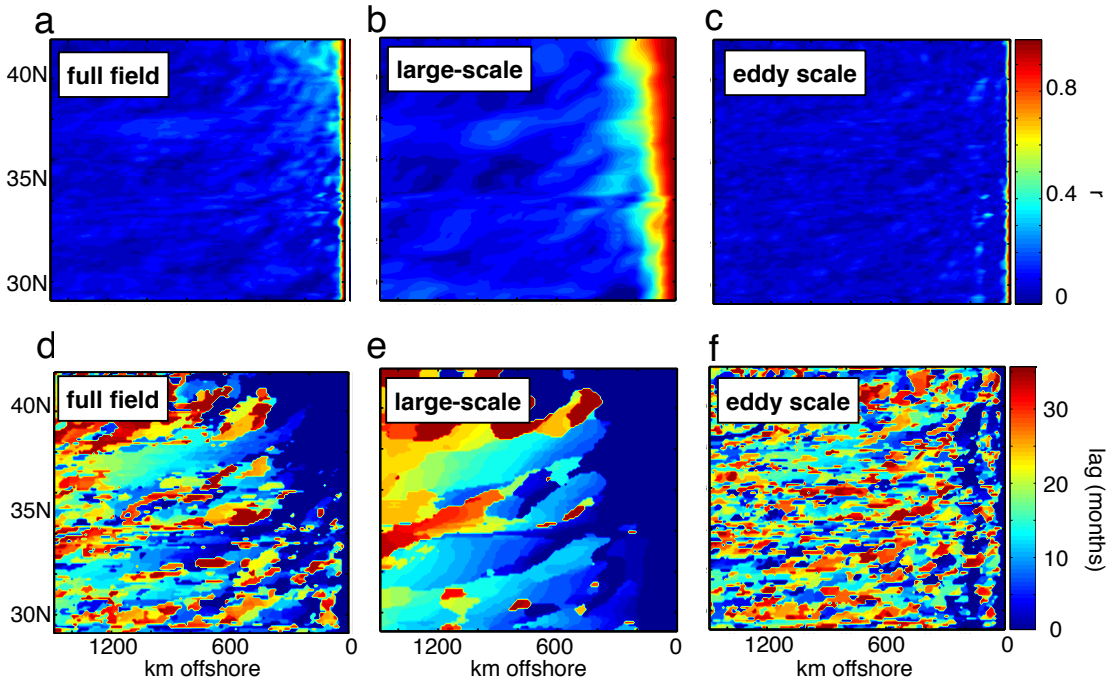

Figure 8 - (a) Maximum correlations over lags of up to three years between offshore and coastal v_e using the full v_e field, (b) the spatial-lowpassed field, and (c) the highpassed field. (d), (e), and (f) The the corresponding lags, in months, for which this maximum correlation is found.

To determine the extent to which a stationary wind stress curl pattern drives v_e, we first compute an offshore profile of the spatially non-smoothed alongshore flow (i.e. large-scale + mesoscale) (Figure 9A) using the normalized coordinate system shown in figure 6. We then compute a single time index of equatorward transport by taking a spatial mean value between 225 and 1100 km offshore, where v_e is strongly

negative (e.g. the core of the CCS southward alongshore flow) (Figure 9B). This index represents the large-scale alongshore equatorward transport associated with the CCS, but pointwise correlations between this index and v_e show that the velocity field is dominated by eddy-scale variance (Figure 9C). To determine the spatial scales that this index most effectively characterizes, we compute correlations between the index and v_e averaged zonally across the CCS region (Figure 9C between dotted lines), and averaged meridionally in bins of varying length L_y (Figure 9D). When L_y is less than 200km, eddies dominate. When L_y is greater than 500km alongshore transports become coherent. This large-scale component of transport variance is largely stationary (Figure 8B,E), and its dynamics should follow the stationary wind stress curl balance described in section 1. Time series of this index for the OBC 1 and no OBC run are strongly correlated at 0.6 (not shown). The large amount of shared variance in mean v_e across both runs indicates a strong deterministic component derived from their common NCEP wind stress forcing.

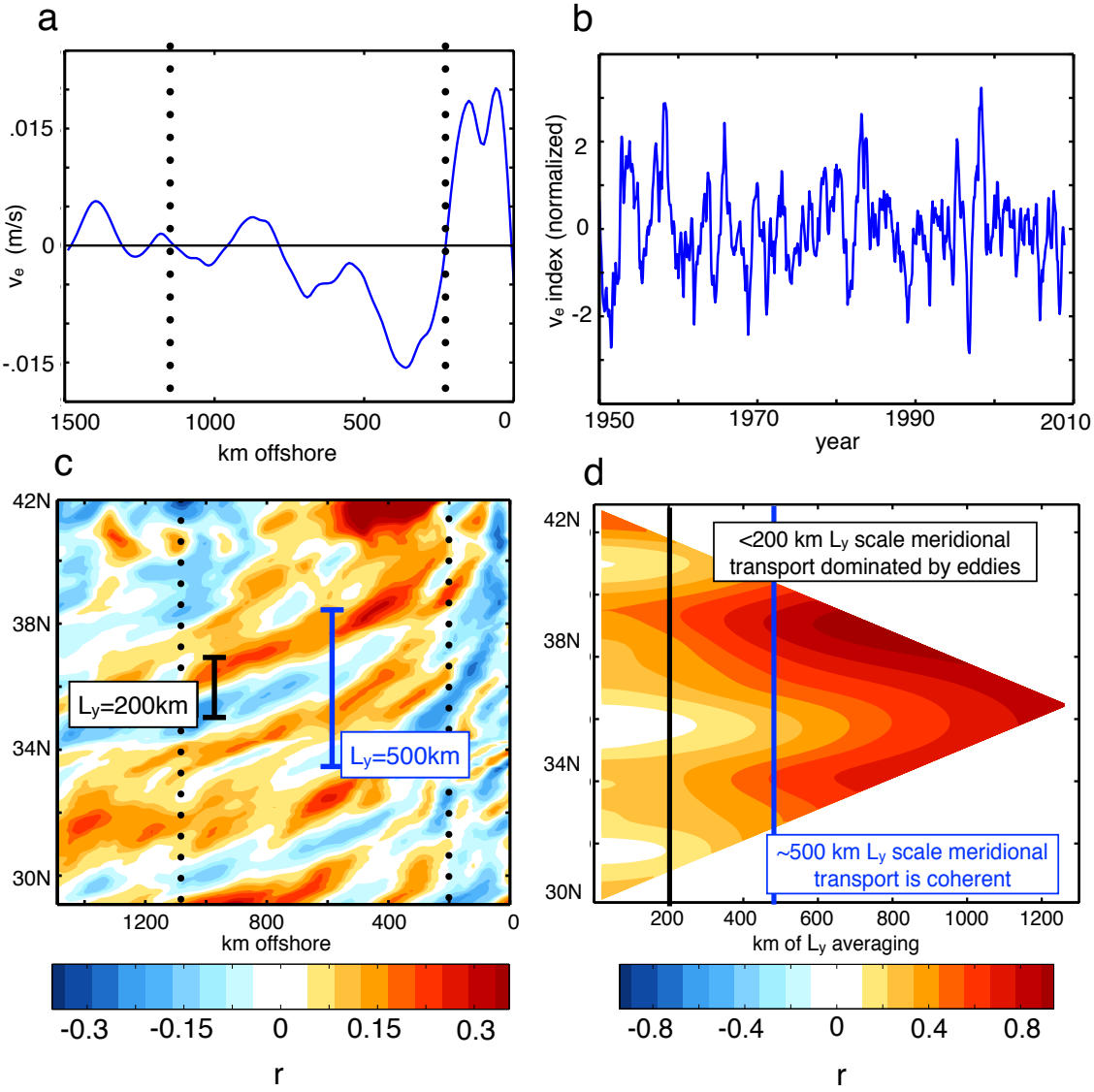

Figure 9 - (a) The offshore profile of v_e obtained from a meridional average. Dotted lines show the range over which our transport index is taken. (b) shows this time-varying transport index. (c) is a pointwise correlation between this index and v_e. (d) shows the correlation between the index and v averaged into meridional bins of varying width L_v.

Projecting the v_e index onto local NCEP wind stress curl (Figure 10A) produces a strong large-scale cross-shelf gradient. Projecting this resulting gradient pattern onto the time dependent curl anomaly yields an index which we assume is an effective index of the wind forcing term in equation 4. It can accordingly be used to drive an autoregressive order-1 (AR1) model to hindcast both an index of large-scale stationary SSH gradients as well as the v_e index (Figure 10B). The AR1 model hindcast (with a decorrelation time scale of 8 months) is strongly correlated (R=0.7) with the time dependent SSH index as well as the v_e index in both OBC 1 and no OBC integrations. This confirms that the majority of deterministic large-scale meridional transport variance is driven by local wind forcing. The cross-shelf wind stress curl gradient and its associated Ekman pumping yield anomalous SSH gradients and associated large-scale geostrophic anomalies.

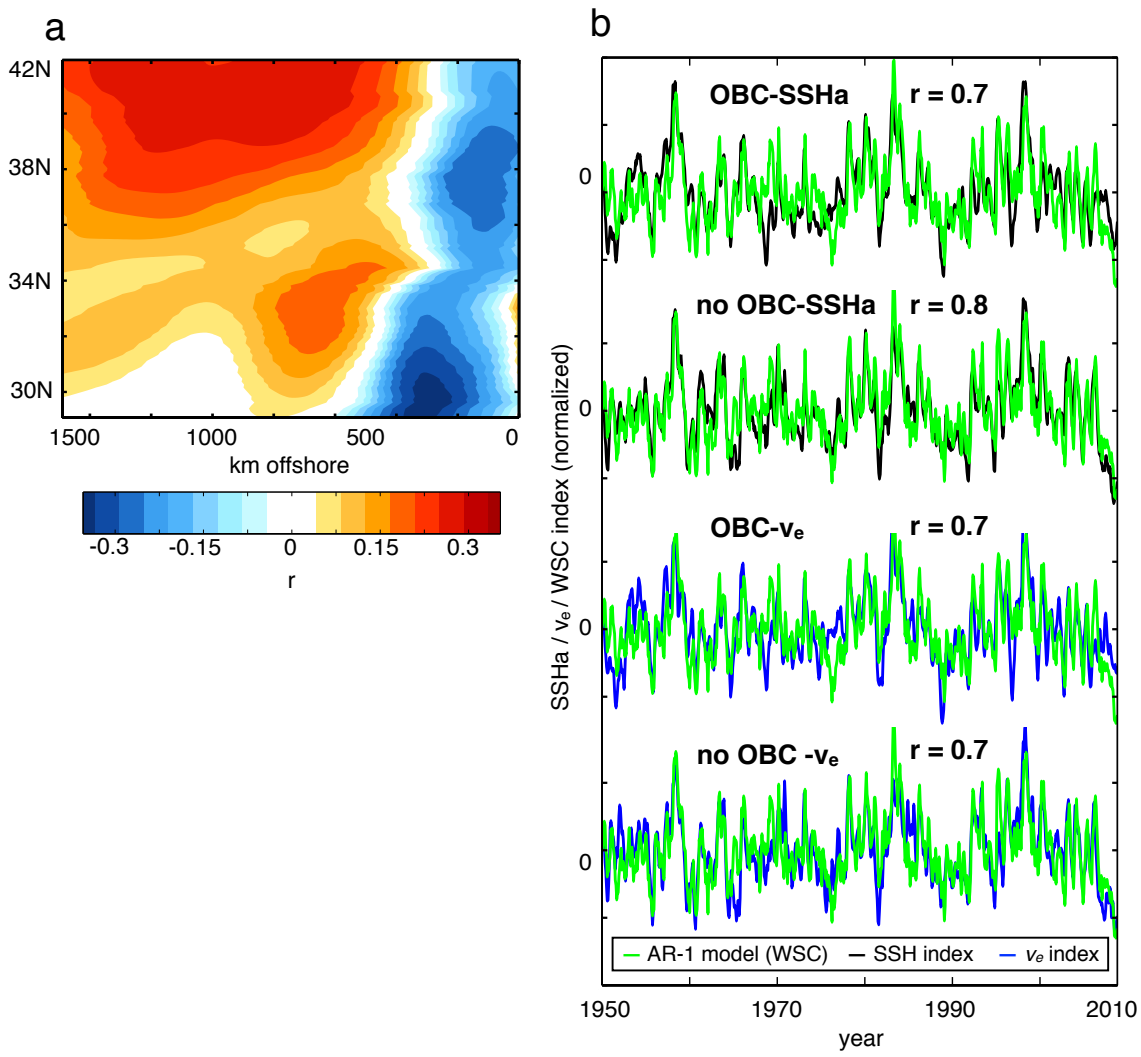

Figure 10 - (a) correlates the transport index with pointwise wind stress curl. (b) compares a time series of an autoregressive order-1 model driven by this wind stress curl pattern with an index of the stationary large-scale cross-shelf SSH gradient, as well as the v_e transport index for both integrations.

The pattern of wind stress curl cross-shelf gradient that drives the meridional transport (Figure 10A) is very similar to the spatial projection of the first principal component (PC) of wind stress curl in this region (Figure 11A), and this PC correlates with the wind stress curl index at 0.9 (Figure 11B). The similarity of the structure of the projection of this PC to the mean wind stress curl (Figure 11C) suggests that the primary mode of wind stress curl variability (and the optimal driver of alongshore current variability) is a strengthening/damping of the stationary mean pattern.

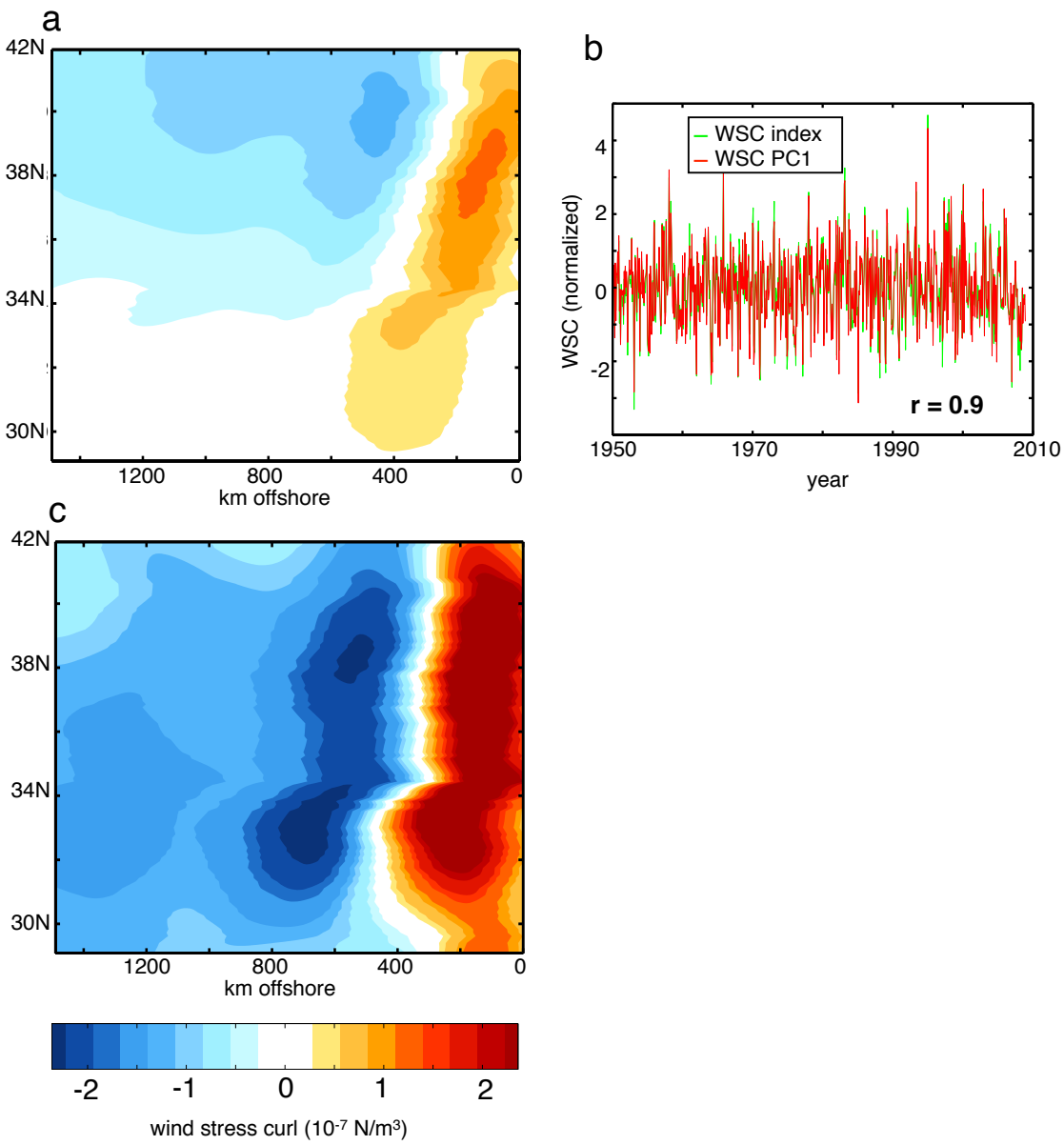

Figure 11 - (a) The projection of the first PC of CCS wind stress curl onto the full field. (b) comparison between this PC (PC1) and the wind stress curl gradient index. (c) the local mean wind stress curl.

From the previous analysis we conclude that it is this dominant mode of local wind stress curl variability that forces alongshore transports in the CCS, rather than remote CTW's. This pattern of curl is not, however, fully independent of the ENSO atmospheric bridge (Alexander, 1992). During a positive ENSO phase the atmospheric teleconnections to the Aleutian Low project onto this cross-shelf pattern of the wind stress curl and drive the oceanic response of the Pacific Decadal Oscillation (PDO) in the CCS (Alexander, 1992; Mantua et al., 1997; Alexander et al., 2002). The PDO has been linked to changes in alongshore transport along the Pacific eastern boundary (Chhak et al., 2009) and a fraction of the local CCS meridional transport variability v_e is captured by the PDO (R=0.4, Figure 12).

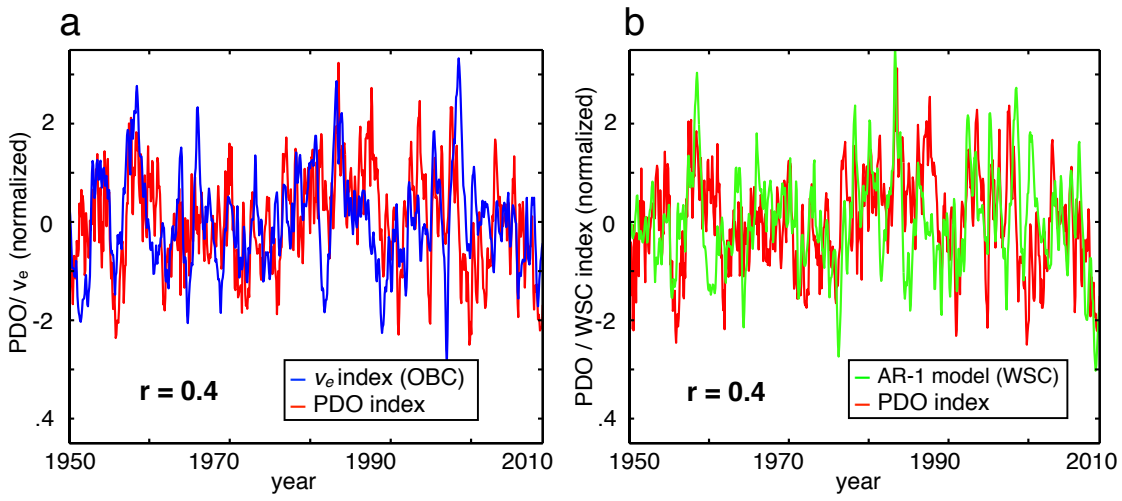

Figure 12 - (a) The PDO index compared with the v_e index (positive values indicate poleward transport). (b) The PDO index compared with the wind stress curl gradient index.

Although these analyses suggest that Rossby waves may play only a minor role in modulating the alongshore transport in the CCS we re-examine this question

using a simple Rossby wave model to hindcast and separate the offshore SSHa and v_e variance associated with remote wave forcing and local atmospheric forcing.

3.4 Rossby wave hindcast

First we used a simple forced Rossby wave model to reconstruct the large-scale sea surface height variability assuming that local winds are the primary driver of SSHa in the CCS. This hindcast employed NCEP wind stress curl records and an equation adapted from Fu and Qiu (2002),

$$h_{curl}(x,t) = k_1 \int_{x_e}^{x} \nabla \times \tau(x', t - \frac{x - x'}{c}) dx' \quad (5)$$

which integrates sea surface height h_{curl} with the curl of wind stress τ over a distance x' assuming a Rossby wave phase speed c (in a long wave approximation). k_1 is arbitrary, given that only the time variability of anomalies is relevant to the analysis. Meridional currents resulting from winds can be computed similarly assuming geostrophy (k_2 is again arbitrary).

. $$v_{curl}(x,t) = k_2 \int_{x_e}^{x} \nabla \times \frac{\partial \tau}{\partial x}(x', t - \frac{x - x'}{c}) dx' \quad (6)$$

This equation can be generalized to an alongshore-oriented velocity as

$$v_{curl}(x,t) = k_2 \int_{x_e}^{x} \nabla \times \frac{\partial \tau}{\partial n}(x', t - \frac{x - x'}{c}) dx' , \quad (7)$$

where n represents a vector normal to the coast. Equivalent data sets for coastally originating Rossby waves were computed based on the assumption that on monthly time scales, variance in coastal SSH and v_e is dominated by CTW dynamics: The SSHa variability arising from Rossby waves originating from the coast (h_{coast}) is expressed as

$$h_{coast}(x,t) = h(x_e, t - \frac{x - x_c}{c}) \tag{8}$$

while the corresponding alongshore anomalies are expressed as

. $$v_{coast}(x,t) = v(x_e, t - \frac{x - x_c}{c}) \tag{9}$$

We then computed correlations between these data sets and model output values for the large-scale (>200km) SSH and v anomalies.

Essential in constructing both of these data sets is the speed of baroclinic Rossby waves. Observed phase speeds in the ocean are between one and two times those predicted by theory, and this ratio increases with latitude. Killworth et al. (1997) argued that baroclinic zonal flows were the cause. They calculated phase speeds for the first baroclinic Rossby wave mode using observed temperature and salinity. Values for the CCS region were found to be between 1 and 3 cm/s. Dottori and Clarke (2008), however, observed dynamic height anomalies propagating through the CalCOFI sampling region at 4.1 cm/s, yet faster than a Rossby wave speed with the

mean cross-shelf flow included. In our reconstructions of SSHa we used the Rossby wave speed observed in our ROMS data for a given latitude and frequency band, which vary between 3.9 and 1.9 cm/s, and are thus consistent with the Dottori and Clarke (2008) estimate.

After reconstructing synthetic data sets h_{curl} and h_{coast} using equations 5 and 8, respectively, correlations were computed between large-scale SSHa and h_{curl} and SSHa and h_{coast} (Figure 13). Variance due to wind stress curl increases at higher latitudes and in the offshore direction, and variance from CTW dynamics increases near shore and at low latitudes. The inclusion of equatorially originating CTW's (through the OBC) also increases this explained variance. It is also clear from the reconstructions that there are regions (red circles in Figure 13A,B) where the Rossby wave model fails to capture the variance in SSHa. These "corridors" are located in regions where there is strong eddy shedding in the model associated with capes in the coastline (e.g. south of Pt. Conception ~34°N and off Pt. Arena ~40°N north of San Francisco).

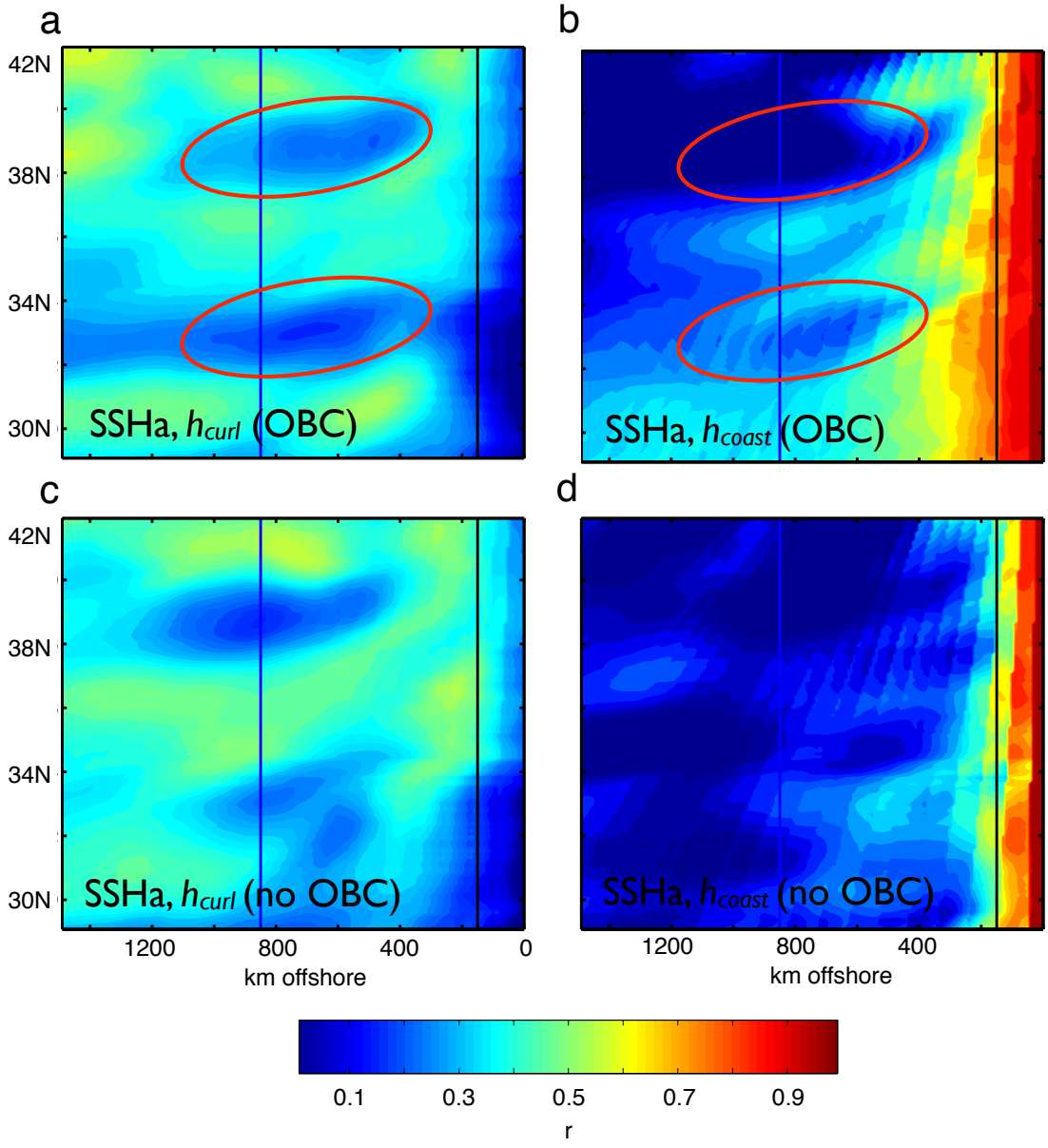

Figure 13 - (a) Correlations between SSHa derived from NCEP wind stress curl and SSHa using OFES boundary condition (OBC). (b) Correlations between Coastal SSHa and offshore SSHa using OFES boundary conditions. (c) and (d) Corresponding plots for the no OBC boundary condition. All assume a Rossby wave speed that linearly decreases with latitude.

The no OBC simulation does show a significant fraction of variance explained by coastally originating Rossby waves. This can be attributed to CTW anomalies excited within the computational domain, indicating that “semi-local” forcing also plays a role in SSH variance.

Corresponding plots were computed to determine the relative dominance of remote and local forcing in modulating v_e. First we reconstructed a v_{curl} using equation 6 and a v_{coast} using equation 8 and computed correlation maps (Figure 14A,C). To first order, the overall hindcast skill of the Rossby wave model is significantly reduced, consistent with the findings of section 3.3—that most of the meridional velocity variance is not explained by simple Rossby wave dynamics. Variance explained by CTW dynamics is further confined to a narrow nearshore region, both with and without the inclusion of equatorially generated CTW’s (Figure 14B,D).

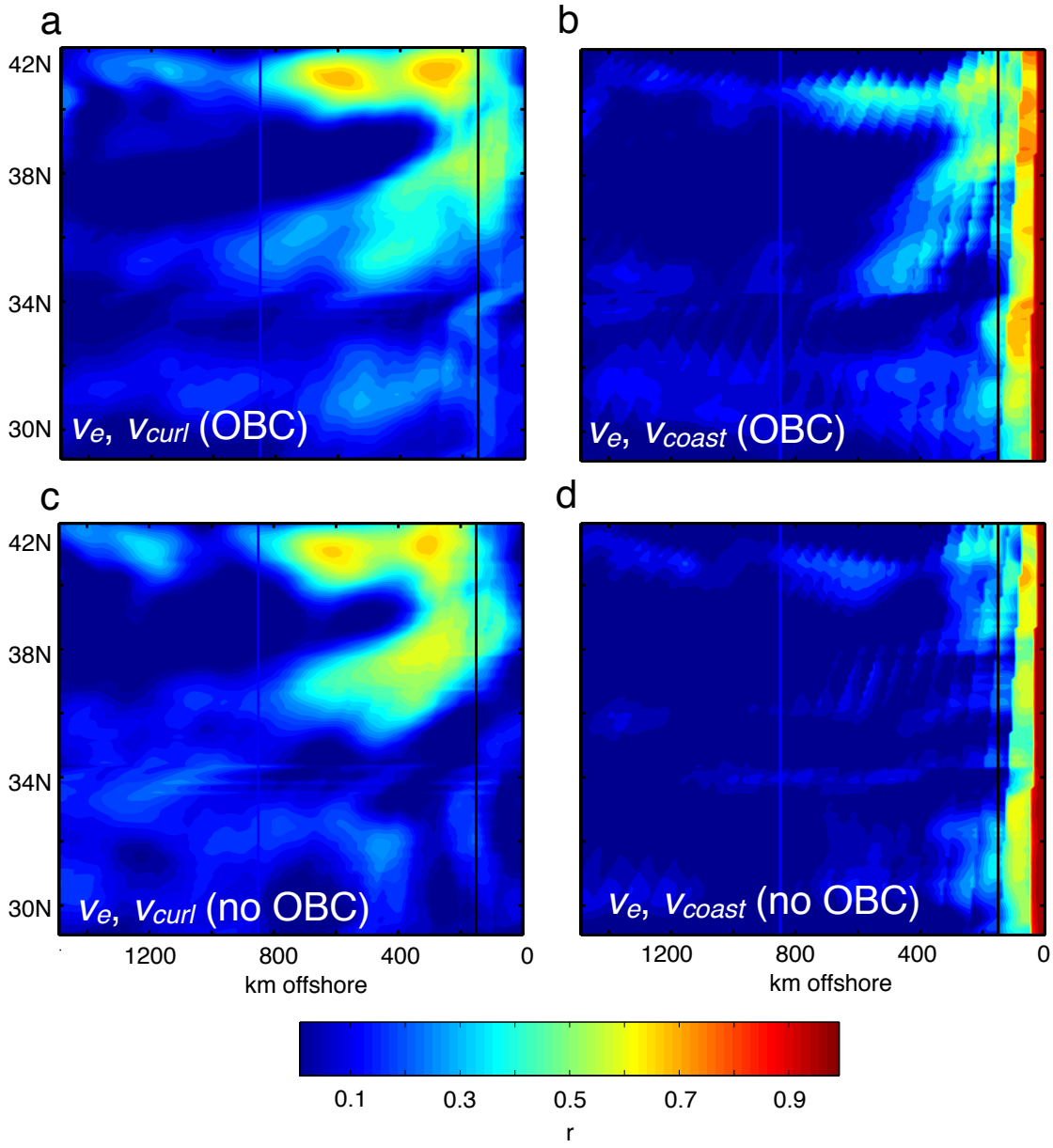

Figure 14 - (a) Correlations between v_e derived from NCEP wind stress curl and v_e using OFES boundary conditions. (b) Correlations between coastal v_e and offshore v_e using OFES boundary conditions (OBC). (c) and (d) Corresponding plots without the OFES boundary condition (no OBC).

This confirms the principal result of the previous sections- namely, that CTW variance is only effective in driving SSHa. Alongshore currents are driven primarily by local wind stress curl. This directly contradicts the results of Dottori and Clarke (2008; 2009), suggesting that remote forcing modulates large-scale alongshore transports interannually only by means of the atmospheric teleconnection.

While we have developed a model of large-scale current forcing with considerable explanatory power, we have so far neglected to determine what fraction of transport this actually represents. Using the filtering method described in Section 3.3, SSHa and v_e variance can be separated into large-scale and mesoscale components to establish their relative magnitudes and spatial distribution (Figure 15). Of particular note is that large-scale SSHa variance is much stronger than the mesoscale, while the opposite is true for v_e. This means that large-scale transport variability is a relatively small fraction of overall variance. Without understanding the mechanisms underlying mesoscale variability, we have an incomplete picture of the forcing of CCS transports. This motivates the following chapter.

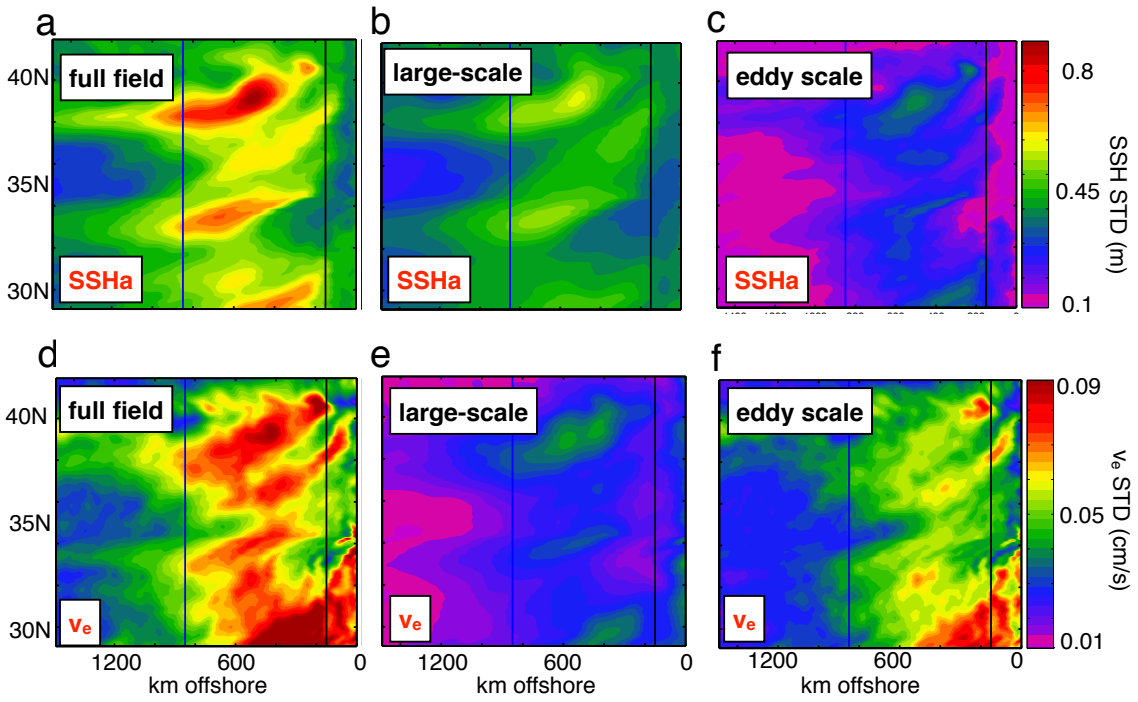

Figure 15 - (a) SSH standard deviation from our OFES boundary condition integration and corresponding plots for (b) spatial highpass (< 200km) and (c) lowpass (> 200km). (d), (e), and (f) are corresponding maps for v_e standard deviation.

Chapter 4: Interannual variance and forcing of CCS mesoscale eddies

4.1: The structure and variance of the CCS eddy field

Eddies play a large role in local horizontal and vertical mixing, and their nonlinearity effectively entrains and transports physical and biological tracers offshore (Chereskin et al., 2000; Cornuelle et al., 2000; Gruber et al., 2006; Combes et al., 2013). CCS eddies may also contribute to the generation of Eastern boundary subsurface temperature and salinity anomalies, which have been shown to propagate into the equatorial thermocline (Fukumori et al., 2004), possibly feeding back onto climate. While CCS eddy formation is a chaotic process and therefore to a large extent intrinsically variable (Marchesiello et al., 2003), the underlying conditions for instability are forced seasonally, and possibly on longer time scales as well (Strub and James, 2000; Stegmann and Schwing, 2007; Chaigneau et al., 2009; Kurian et al., 2011). The aim of this section is to determine what proximate physical mechanisms modulate eddy activity on interannual and decadal frequencies, and what local and basin-scale climate processes are their most effective drivers.

Satellite observations have established the general patterns of CCS eddy activity (Kelly et al., 1998; Stegman and Schwing, 2007; Keister and Strub, 2008). A map of the variance of relative vorticity derived from AVISO altimetry (Figure 15A) shows an offshore band of strong eddy-scale variability. Eddy kinetic energy (EKE) has a distinct seasonal cycle, peaking in late summer/early fall (Marchesiello et al., 2003).

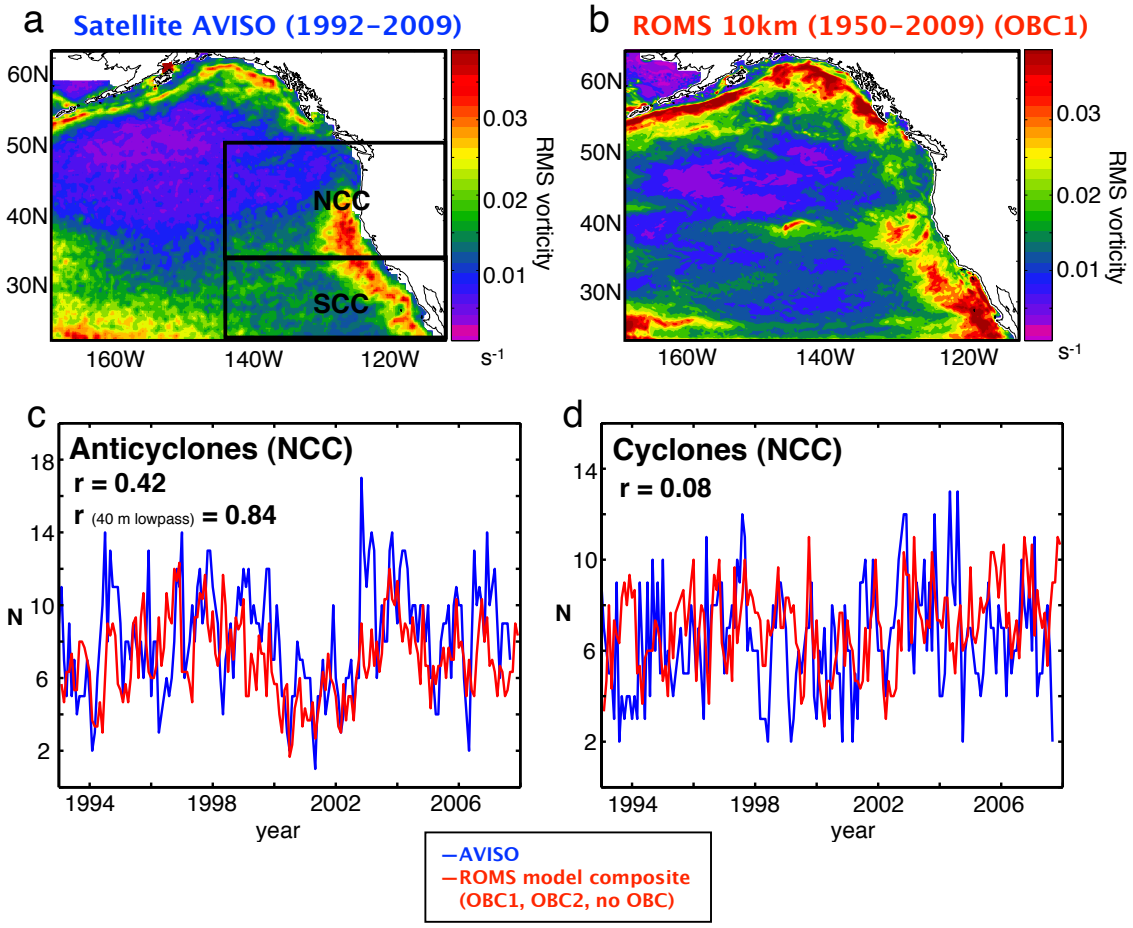

Figure 16 - (a) Relative vorticity variance as observed by AVISO altimetry. (b) The same variance derived from our OBC1 integration. Northern California Current (NCC) region eddy count (*N*) time series derived from AVISO observations using the SSHa contour method (blue line), and a model composite from our three ROMS integrations (OBC1, OBC2, no OBC) using the *W* method (red line) for (c) anticyclones and (d) cyclones. Correlations are given, with an additional value for the correlation between modeled and observed NCC anticyclones after a 40-month lowpass.

Few eddies are formed or propagate north of 43 degrees, possibly as a result of the detachment of the alongshore upwelling jet (Stegman and Schwing, 2007). South of this boundary and north of the Southern California Bight (SCB), eddies are formed in a narrow region just offshore of the 1000m isobath (Kurczyn et al., 2012). They then propagate offshore at an average rate of 1.5 km/day (roughly the same speed as short Rossby waves) (Chelton et al., 2007; 2011; Kurian et al., 2011). As eddies move westward, they tend to grow horizontally and exhibit the classical kinetic energy "length cascade" (Peltier and Stuhne, 2002). They also can become entrained in and advected meridionally by the California Current (Kurian et al., 2011).

Observational and modeling studies have confirmed that CCS eddies fall into two general categories: deep-core anticyclones (with an enstrophy maximum at roughly 400m depth) and surface-core cyclones (Brink et al., 2000; Chereskin et al., 2000; Jerónimo and Gómez-Valdéz, 2007; Kurian et al., 2011). There is a substantial bias north of the SCB towards the production of anticyclones (Stegman and Schwing, 2007). While there is some indication that cyclone and anticyclone formation have distinct seasonal cycles (Stegman and Schwing, 2007), other studies have concluded that there is little seasonality in the formation of all but the longest-lived eddies (Chaigneau et al., 2009; Kurian et al., 2011).

It has long been known that alongshore wind forcing generates the distribution of surface mesoscale energy in the CCS on seasonal time scales (Pares-Sierra et al., 1993). There is also a body of work indicating that CCS eddies are formed as a result of both baroclinic instability within the poleward-flowing undercurrent and surface velocity shearing (Chereskin et al., 2000; Cornuelle et al.,

2000; Marchesiello et al., 2003; Jerónimo and Gómez-Valdés, 2007) Eddy activity may also be modulated by the spatial variability of the alongshore upwelling jet (Barth et al. 2000).

Cyclones are also associated with local vertical mixing, and while they may reduce overall productivity in EBC's (Gruber et al. 2011), by bringing nutrients into the euphotic zone they can also serve as local "hot spots" for phytoplankton growth (McGillicuddy et al., 2007). Anticyclones, in contrast, are more effective in transporting tracers offshore (Cornuelle et al., 2000; Combes et al., 2013). The fact that cyclones and anticyclones possibly have different proximate forcing mechanisms, mixing properties, ecosystem roles, and spatial distributions necessitates an approach that considers them separately.

The short length of satellite data has generally made a comparison between eddy observations and basin-scale climate indices difficult, but there have been some attempts to tie mesoscale activity to individual climate events. Keister and Strub (2008) used wavelet analysis of satellite-derived SSHa to quantify eddy kinetic energy. They found that EKE increased in the fall preceding the 1997/1998 and 2002/2003 El Niño events, but was then suppressed the following winter. In the case of the 1997/1998 event, energy did not return to its mean state until mid-2001. The 2002/2003 event had a weaker effect on EKE, possibly due to stronger teleconnected alongshore winds. They also reported a weakly significant correlation between EKE and the PDO, associated with low-frequency stratification anomalies and attendant available potential energy (APE) modulation.

In this chapter, we use our hindcast ensemble (OBC1, OBC2, no OBC) to determine what fraction of eddy variance was forced externally. The atmospheric forcing dynamics and accompanying ocean processes that lead to this

deterministic response are then diagnosed. In chapter 3, we concluded that coastal-trapped wave (CTW) energy associated with ENSO (and therefore the ENSO remote signal) was largely attenuated north of this SCB. For this reason, in this work the CCS was divided into two regions: a Northern region between 35° N and 50° N (NCC), and a Southern region between 25° N and 35° N degrees (SCC) (Figure 16A).

4.2 Counting mesoscale eddies with the Okubo-Weiss parameter

There are a number of methods for counting mesoscale eddies within a given region of the ocean. A detailed analysis of the advantages and pitfalls of each is given in Kurian et al. (2011). All carry a risk of false positives, underestimations, and misdiagnosis of eddy properties (radius, strength, nonlinearity, etc.). Our principal interest is in the development of robust indices of cyclone and anticyclone activity, rather than in diagnosing eddy properties. This, along with the computationally demanding approach of using three separate model runs, makes counting contours of the Okubo-Weiss parameter (W) (Okubo, 1970; Weiss, 1991) the most attractive option for our ROMS model output (Isern-Fontanet et al., 2003; Chelton et al., 2007). W is given as the difference between the squares of the strain (normal and shear) and the vorticity (Isern-Fontanet et al., 2003).

$$W = \left(\frac{\partial u}{\partial x} - \frac{\partial v}{\partial y}\right)^2 + \left(\frac{\partial v}{\partial x} + \frac{\partial u}{\partial y}\right)^2 - \left(\frac{\partial v}{\partial x} - \frac{\partial u}{\partial y}\right)^2 \quad (10)$$

An assumption of nondivergent, planar flow allows for a simplification to

$$W = 4\left(\left(\frac{\partial u}{\partial x}\right)^2 + \left(\frac{\partial v}{\partial x}\right)\left(\frac{\partial u}{\partial y}\right)\right) \tag{11}$$

For the most effective characterization of mesoscale activity, W was computed with spatial-highpassed surface monthly mean u and v. This highpass was achieved by employing a circular spatial running mean of 200 km diameter to create an effectively lowpassed field, which was then subtracted from the full record. The resulting highpassed velocity fields were interpolated to a resolution of 5km in order to lessen potential noise from finite-differencing. To develop eddy count time series we summed the number of occurrences of a specific closed contour within the field. We chose a contour that gave us counts in agreement with previous observations, visual inspection, and counts derived from continuous-contouring schemes. Eddy polarity was determined using the depth of the vorticity maximum and the sign of a similarly highpassed SSHa field at the eddy center.

The W-contouring method has a well-documented bias toward false positives, with other mesoscale and sub-mesoscale features counted as eddies (Chaigneau et al., 2008). For this reason, we included a mechanism to exclude features that are insufficiently circular, similar to that of Kurian et al. (2011). This requires the calculation of the ratio of the variance of a contour from a circle of its average radius to the area of this circle. If this “shape error” exceeds 35%, the contour is excluded from the eddy count. In practice, the interannual variability of eddies tended to be insensitive to shape error criteria between 20 and 50%.

AVISO altimeter data was also employed in order to validate the model-derived eddy-count time series. Although an assumption of geostrophy would allow for computation of W contours from SSHa, the low resolution of the data (around 30km) means that the three finite differencings required would likely generate excessive noise (Chelton et al., 2011) and possibly mask some small eddies. Here we counted closed contours of spatial-highpassed SSHa (Stegman and Schwing, 2007 Chaigneau et al., 2008; Chelton et al., 2011) and included a more lenient shape error criterion of 45%.

Correlation analysis is used extensively throughout this section, with time series of varying lengths and respective autocorrelations. Significance was determined using a Monte Carlo method similar to one described in Di Lorenzo et al. (2009). PDF's of correlation coefficients used for comparison were computed with two sets of 3000 realizations of red-noise time series. These red-noise time series had identical lengths and autoregression coefficients to those of the original time series being correlated. The original correlation coefficient was then compared to this PDF to determine percent significance.

4.3: Eddy count statistics (NCC)

Using the W eddy-count method described previously, we developed eddy count time series from each of the three integrations in the NCC range. These time series share a substantial amount of variance. The three respective correlations between nonseasonal monthly counts derived from the three model runs in anticyclones and cyclones were averaged, yielding $r = 0.30$ for anticyclones and r

= 0.22 for cyclones, indicating a substantial portion of shared (i.e. deterministic) variance.

Comparison between a nonseasonal composite eddy count time series derived from all three integrations and nonseasonal eddy counts derived from AVISO satellite altimetry (using the SSHa contouring method) (Figure 16C,D) shows that the stationary statistics are reproduced. The correlation between observations and the composite anticyclone count is r = 0.42, indicating substantial agreement. The corresponding value for cyclones is much lower, at r = 0.08, but this is consistent with the increased intrinsic variance in cyclones found in the ensemble. In order to validate the spatial patterns of model eddy formation, we developed contour plots of eddy activity by placing normal distributions at each counted eddy location and taking the time mean, providing a probabilistic view of eddy spatial distribution (Figure 17A,B). Comparison with maps of eddy activity derived similarly from AVISO SSHa data (Figure 17C,D), shows a general agreement in areas of eddy concentration, but with some significant differences. Both indicate that eddy activity is strongest in a region between 100 and 700km offshore and south of 43° N, but modeled eddies are most concentrated in the northern half of this range. Model- and observation-derived maps, especially for anticyclones, both show a strong pattern of offshore propagation, but the latitudinal axis along which eddies detach differs. AVISO data shows distant offshore eddies along 37° N, while modeled eddies are confined to an axis of 40° N. In both cases, this propagation supports a hypothesis that eddies have little impact on the mean background flow, and that an approach that treats eddy formation as a forced, linear process is appropriate.

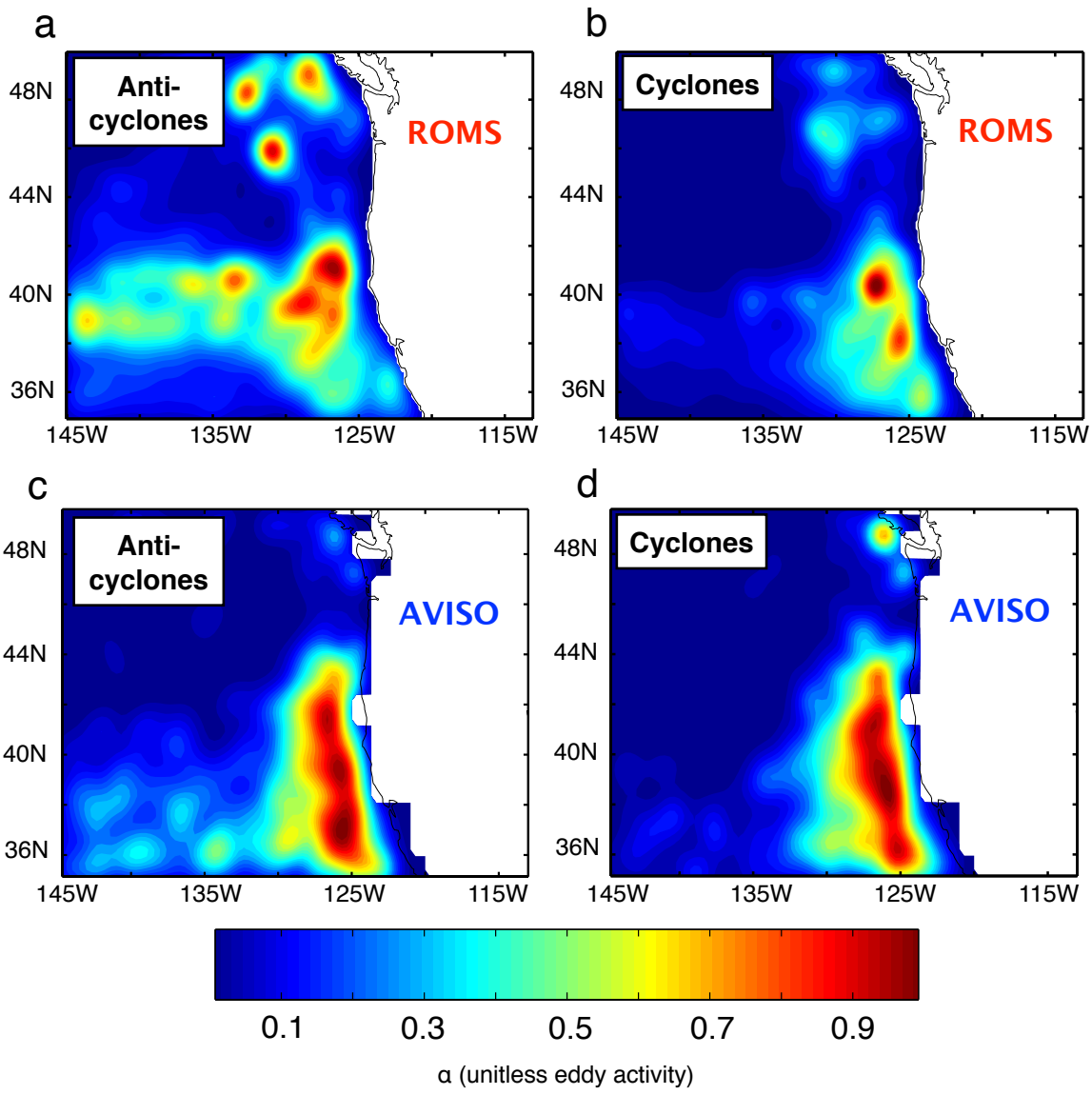

Figure 17 - Composite maps of ROMS-derived eddy activity (α) in the NCC region for (a) anticyclones and (b) cyclones. Corresponding maps of eddy activity from AVISO altimetry for (c) anticyclones and (d) cyclones.

Eddy counts were also examined in frequency space. Individual model run anticyclone and cyclone spectra were computed using three 20-year subsamples, along with a model composite (computed as the mean of the three model spectra) (Figure 18A,B). Our null hypothesis- a red noise spectrum with a decorrelation time scale of 3 months- is plotted at the 99% significance level. Both anticyclones and cyclones evince a strongly significant peak at a yearly frequency, indicating that both have a robust seasonal cycle. All other significant frequencies are within a band bounded on the high end by 0.3 yr^{-1} (periods of 40 months or more). Variance within this band is referred to throughout the remainder of this work as "low-frequency." Based on these spectra, we determine that anticyclones have more low-frequency power (26% low-frequency; 12% seasonal), whereas cyclones have more seasonal variability (17% low-frequency; 16% seasonal). All three model runs (in grey) were plotted in the same color to show that not only do they have similar low-frequency power, but evince no notable differences at all. Most significantly, the spectra of OBC1 and OBC2 do not differ substantially from no OBC (the run employing a purely climatological boundary condition). This suggests that in the NCC, equatorial CTW variance does not play a role in low-frequency eddy modulation.

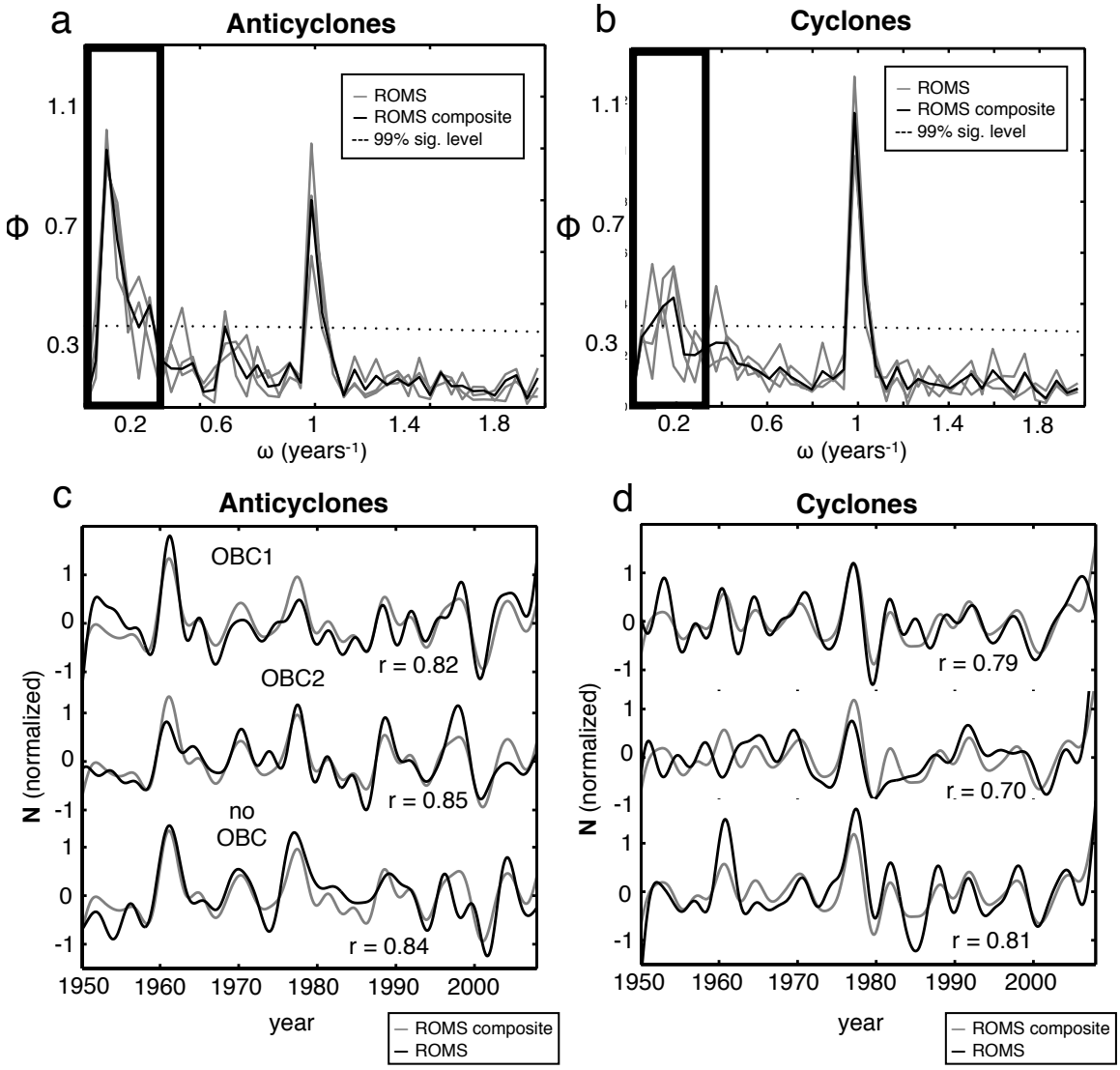

Fig. 18 - NCC eddy count spectra (Φ) of 3 individual ROMS runs (OBC1, OBC2, no OBC; gray lines) and a composite spectrum (black line) for (a) anticyclones and (b) cyclones. The significant frequencies boxed in black are lowpass filtered to give eddy count time series (*N*) of (c) anticyclones and (d) cyclones, for individual model runs (black lines), and a model composite (gray lines).

To further validate the model representation of NCC eddy variance, we compared the respective model composite seasonal cycles of cyclones and anticyclones and found that both evince the canonical late summer/early fall peak in eddy activity (Kelly et al., 1998; Strub and James, 2000; Kurian et al., 2011).

Eddy count time series were detrended, lowpassed (containing periods longer than 40 months), and normalized (to a variance of 1) to isolate modulations of interest (Figure 18C,D). Correlations between individual runs and composites indicate that 25-35% of low-frequency variance in anticyclones is deterministic. Cyclone count correlations are somewhat lower; only 10-25% of cyclone variance is shared.

Lagged correlations between model composite lowpassed cyclone and anticyclone counts reach a maximum of r = 0.73 with cyclones leading by 4 months. With the assumption that this model composite eddy count is the optimum representation of the driven component of eddy variance, this high correlation indicates that they likely share a source of forcing on interannual (rather than just seasonal) time scales. Although considering cyclones and anticyclones separately has been vital in validating model eddy counts and in establishing their respective fractions of deterministic and intrinsic variance, they are likely forced by similar means.

4.4: Diagnostic model of eddy formation (NCC)

Eddy variability in the CCS has been theorized to be driven both by large-scale changes in the baroclinic structure (specifically the vertical stratification in the upper ocean), as well as barotropic modulation of the large-scale flow

(Chereskin et al., 2000; Cornuelle et al., 2000; Marchesiello et al.; 2003; Jerónimo and Gómez-Valdés, 2007). For this reason, we developed two indices of eddy formation, representing both depth-averaged (barotropic) and depth-dependent (baroclinic) components. To determine from what area these indices should be drawn, we computed maps (derived as detailed in section 4.1) of late summer eddy activity (Figure 19A,B), shown in our model (in agreement with observations) to be the season in which most eddies are formed.

The barotropic index was derived from a spatial mean of anomalous alongshore currents derived from each of our model outputs, depth-averaged to 400m to ensure the capture of deep-core anticyclone formation. The record was also horizontally lowpassed at 200km in order to remove any eddy signal. The area over which this mean was taken was an alongshore region between 36° N and 44° N (Figure 19A). This index correlates with the lowpassed model composite anticyclone counts at r = 0.5 (Figure 19C).

The baroclinic index was derived based on the assumption that eddies, especially anticyclones, are formed partially as the result of instabilities within the poleward-flowing undercurrent. The upper boundary of the undercurrent is generally taken as isopycnal 26.5. Anomalous available potential energy should be strongly related to the stratification anomaly, and thus the distance between neighboring isopycnals. The index was computed by calculating the gradient of horizontally lowpassed isopycnal depth in the vertical dimension about 26.5 and taking a horizontal mean in the observed area of eddy formation. This index also correlates with the lowpassed model composite anticyclone counts at R = 0.5 (Figure 19D) at a lag of 9 months.

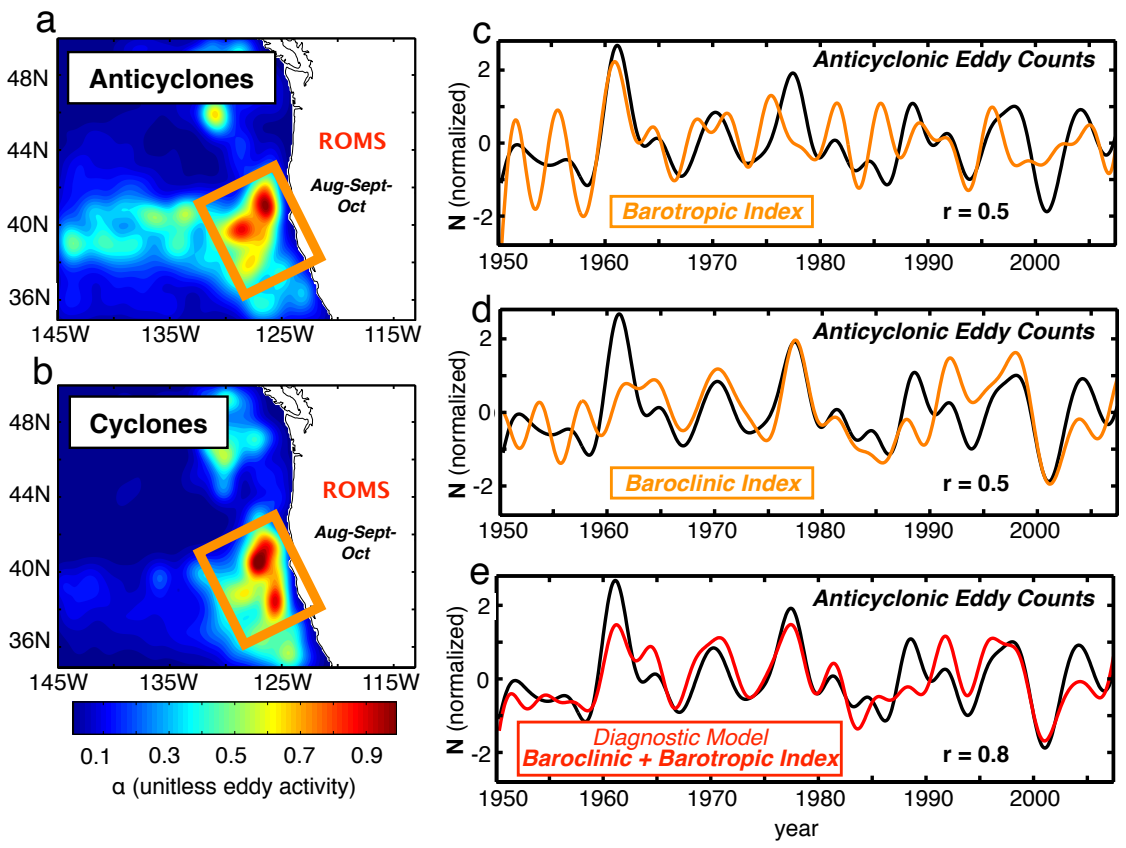

Figure 19- Model composite maps of late summer/early fall (a) anticyclone and (b) cyclone activity (α) in the NCC region along with the areas of physical index averaging (overlaid in orange). The lowpass filtered model composite anticyclonic eddy counts (black lines) compared with (c) the filtered composite barotropic index (orange line), (d) the filtered composite baroclinic index (lagged at 9 months; orange line), and (e) the combined diagnostic model (red line).

Barotropic and baroclinic indices show no significant correlations for lags of up to one year, indicating that they are largely orthogonal and independent. Least-squares analysis provides correlations and lags of maximum correlation between each of these indices and eddy count time series (R = 0.5 at 9 months for the baroclinic index; R = 0.5 at 0 months for the barotropic index). These correlations can then be employed as weighting coefficients in order to combine baroclinic and barotropic indices into a single diagnostic model of potential eddy activity. Correlation of a lowpassed composite (a mean of from all three model simulations) of this diagnostic model with lowpassed composite anticyclone count is a 99% significant R = 0.8 (Figure 19E). Although cyclones have a smaller fraction of forced variance (only 10-15%), this index also correlates well with a lowpassed composite cyclone count at R = 0.7. This index also correlates well with individual runs at between R = 0.6 and 0.8 for anticyclones and between 0.4 and 0.6 for cyclones.

4.5 Wind forcing of eddy activity (NCC)

Spectral analysis indicated that the time-dependent OFES boundary condition added little low-frequency variance to modeled eddy counts. Therefore equatorial CTW influence on NCC eddy activity is minimal; forcing is most likely local and wind-driven. To determine what wind patterns most effectively drive eddy variance, we projected our three-run composite of the diagnostic model onto each point of Northeast Pacific NCEP wind stress curl anomalies. The pattern recovered (Figure 20A) has a cross-shelf dipolar shape across the NCC region, as well as pronounced structure to the north and in the offshore. The patterns of the

respective projections of the separate barotropic and baroclinic indices (not shown) are extremely similar to this pattern, especially in the CCS region. This indicates that while these indices are independent, both are forced by the same wind stress curl gradient.

A further examination of the wind forcing patterns reveals strong similarities between this pattern and the 3rd empirical orthogonal function (EOF) of Northeastern Pacific (NEP) NCEP wind stress curl (Figure 20B). While the first two EOF's of NEP wind stress curl correspond to the Aleutian Low and the North Pacific Oscillation (NPO), respectively, this third mode has not been widely studied and is characterized by strong regional projection along the California Current. While it only represents 8% of variance across the Northeastern Pacific, locally (in the NCC), it accounts for 50% of variance. This 3rd principal component (lowpassed at 40 months) correlates at r = 0.44 with our lowpassed composite diagnostic model (Figure 20C). This relatively low correlation suggests that the regional component of the wind pattern plays an important role, necessitating an index of large-scale cross-shelf wind stress curl gradients in the CCS region (overlaid onto Figure 20B). Correlation between a 40-month lowpass of this index and the lowpassed composite diagnostic model is a 99% significant .62 (Figure 20D). We computed lagged correlations between composite lowpassed eddy counts and the third principal component of NEP wind stress curl (r = .46 at lag = 9 months) as well as the curl gradient index (r = 0.50 at lag = 9 months). The fraction of variance explained by these wind indices (25%) is comparable to the proportion of driven variance in eddy counts (25-35% for anticyclones; 10-25% for cyclones), strongly suggesting that local wind variability drives eddy activity on interannual and decadal scales, just as it does seasonally. Correlations between

these wind indices and eddy counts are not as high as those between eddy counts and our diagnostic model, indicating that a portion of variance of barotropic and baroclinic structures is not derived from wind stress, but either intrinsic or forced by other means.

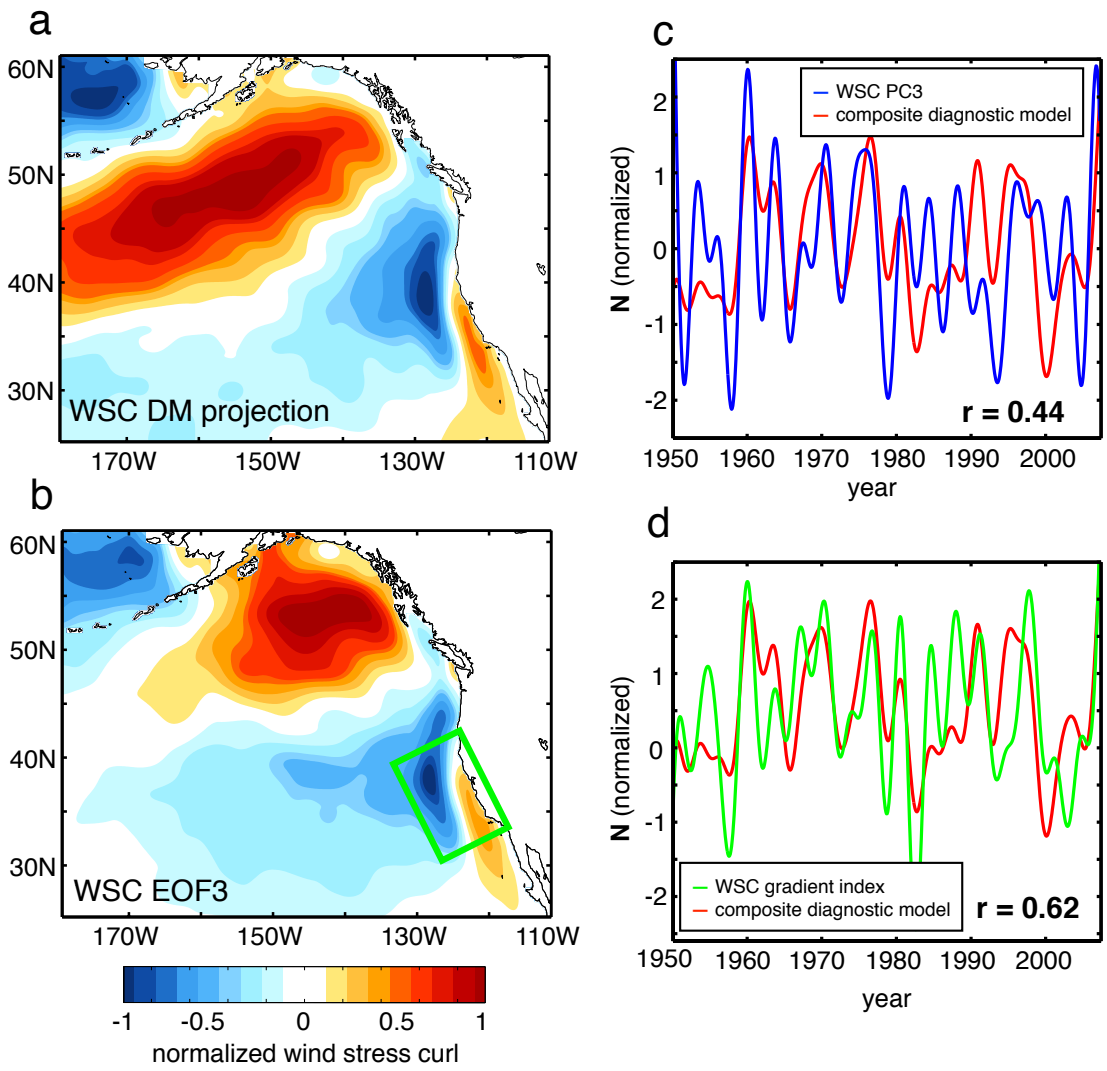

Figure 20 - (a) The projection of the composite diagnostic model (DM) onto Northeastern Pacific NCEP wind stress curl (WSC) with spatial variance normalized to 1. (b) The normalized 3rd EOF of Northeastern Pacific NCEP wind stress curl, with the area over which the wind stress curl gradient index is averaged (green box). (c) The composite diagnostic model (red line) compared with a lowpass filtered time series of the corresponding 3rd principal component of WSC (blue line). (d) The composite diagnostic model (red line) compared with the lowpass filtered wind stress curl gradient index (green line).

4.6 Eddy count statistics (SCC)

Model composite maps of SCC eddy activity from both model runs and observations (Figure 21) evince noticeable inconsistencies, possibly reflecting some of the biases in relative vorticity found near the southeast boundary of the ROMS integration (Figure 16A). Observational records show strong eddy activity extending further towards the SCB and further offshore.

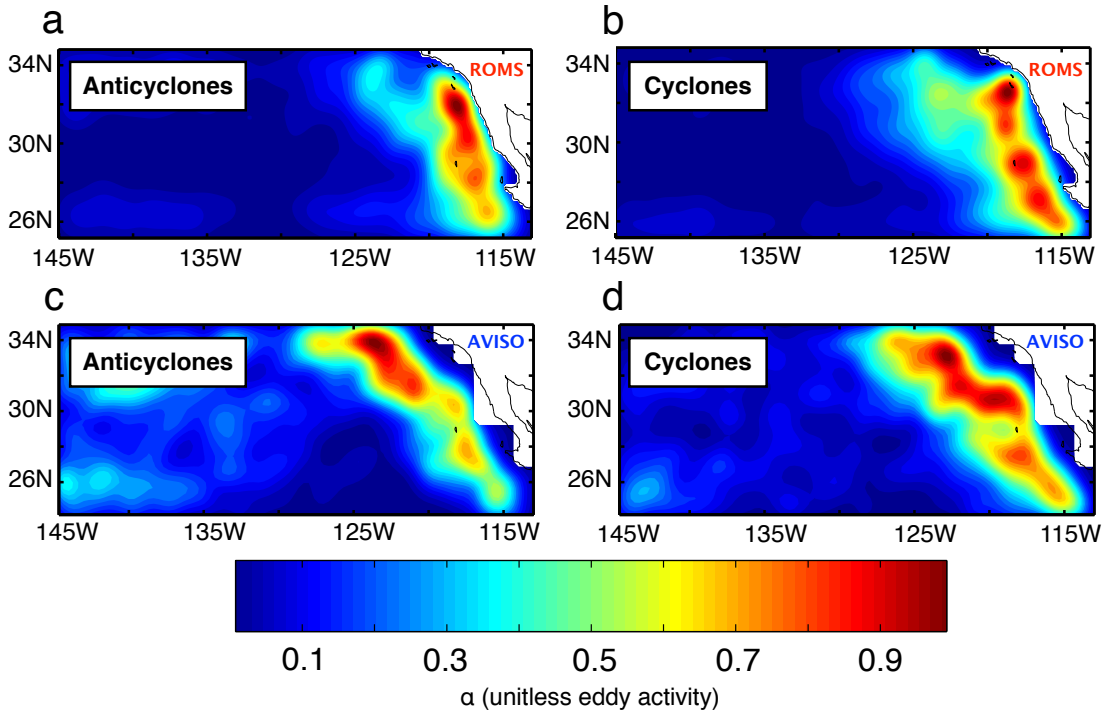

Figure 21 - Model composite maps of ROMS-derived eddy activity (α) for (a) anticyclones and (b) cyclones in the Southern California Current (SCC) region. (c,d) Maps of eddy activity from AVISO altimetry are also computed for anticyclones and cyclones, respectively.

Spectra from the OBC1 and OBC2 runs for anticyclones and cyclones (Figure 22A,B) show much less seasonality than the NCC, but have a narrow band of significant low frequencies, once again bounded at .3 cycles per year. As in the

NCC, these two runs do not noticeably differ. In contrast to the NCC, this low-frequency band is much diminished in the no OBC run (Figure 22C,D), whose spectra conform roughly to red noise. The lack of any band of significant frequencies in this run implies that it is the OFES boundary condition that contributes the significant low-frequency variance to the OBC1 and OBC2 runs, likely by means of CTW activity.

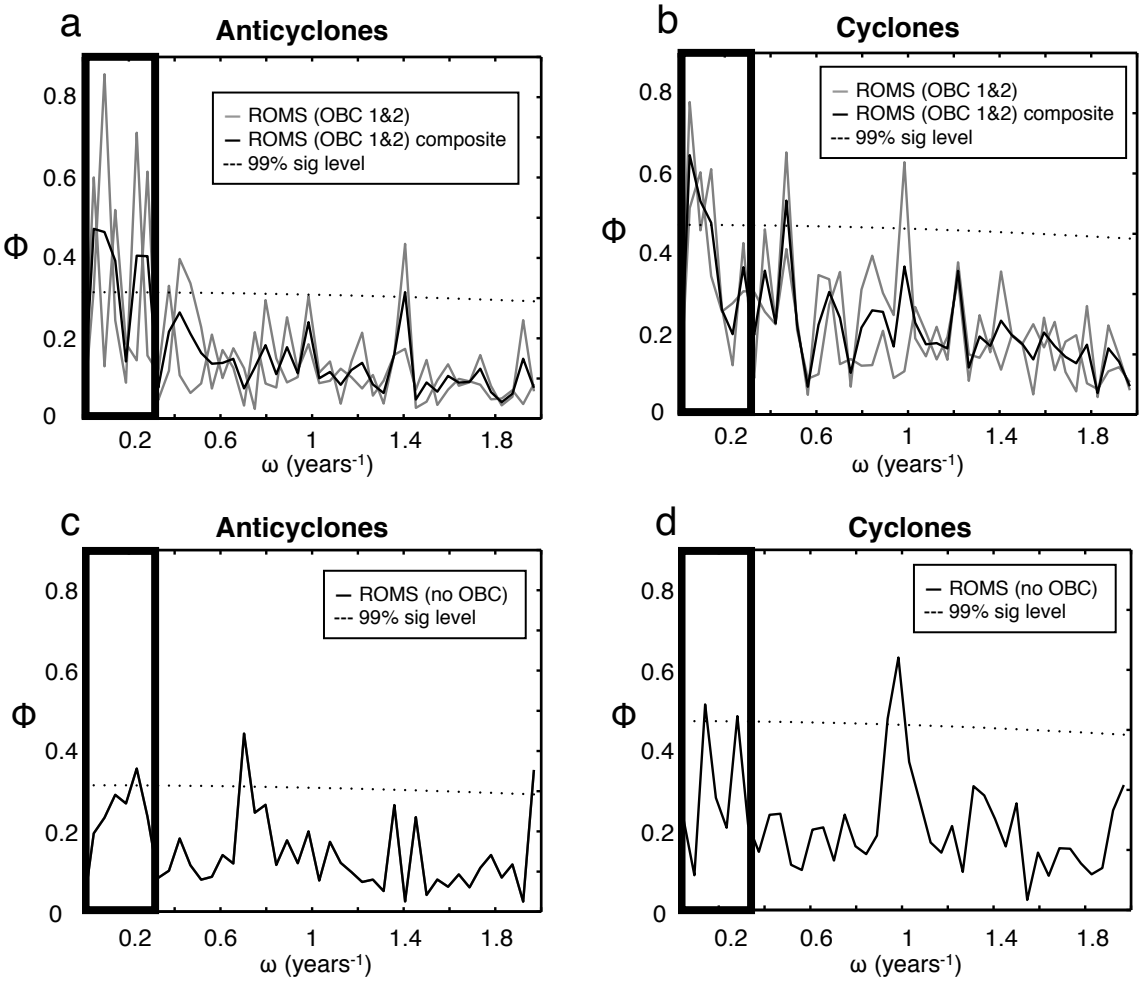

Figure 22 - SCC region eddy count spectra (Φ) for the OBC1 and OBC2 ROMS runs (gray lines) and a composite spectrum from the two (black lines) for (a) anticyclones and (b) cyclones. (c,d) SCC region eddy count spectra (Φ) for the no OBC run (black line) for anticyclones and cyclones, respectively.

Low correlations between 40-month lowpassed eddy count time series and model composites (Figure 23) suggest that only around 10% of low-frequency anticyclone variance is shared, while cyclone variance is virtually completely intrinsic. This is consistent with the spectral characterization of SCC eddy activity as largely a red-noise process.

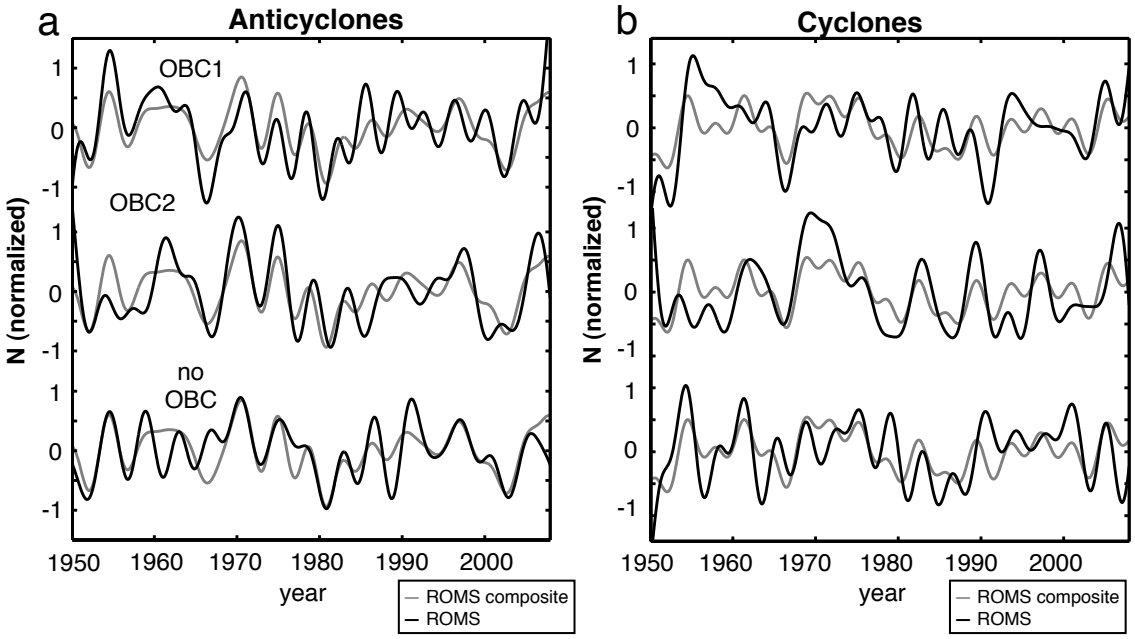

Figure 23 - 40-month lowpass filtered SCC regional eddy count (*N*) time series of (a) anticyclones and (b) cyclones, for individual model runs (black lines), and a model composite (gray lines).

Our explanation for the increased intrinsic variance in modeled SCC eddy counts is as follows. Seasonal maps of SCC anticyclone (Figure 24A) and cyclone (Figure 24B) activity show very little offshore propagation, indicating that modeled eddies are effectively entrained in recirculating currents. This prolonged residence

time for SCC eddies means that they have a much greater effect on the background mean, leading to feedbacks, nonlinearity, and unpredictability. This coupling between large-scale and mesoscale properties would preclude the linear, forced response seen in the NCC.

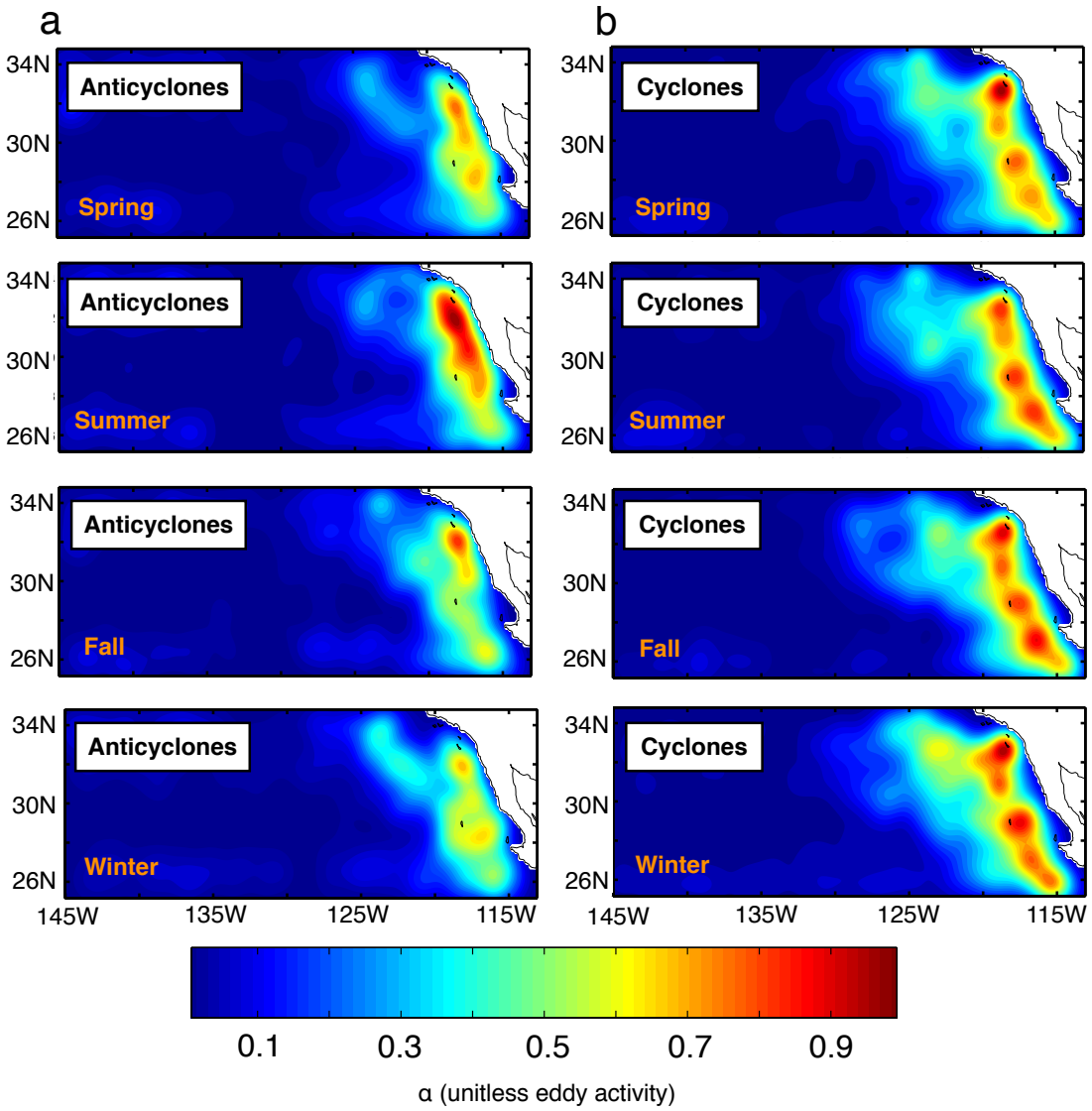

Figure 24 - Seasonal model composite maps of SCC regional eddy activity (α) for (a) anticyclones and (b) cyclones.

Chapter 5: The Mechanisms of striation formation in the Northeast Pacific

5.1: Northeast Pacific striations in models and observations

So far this work has examined the variability of two forms of CCS transport- large-scale alongshore currents and mesoscale eddies. We conclude with a study of a third method- striations. Striations differ from the other two in that they cannot be readily observed on monthly time scales. They only appear in long term (> 2 years) means of zonal currents. It is for this reason that a study of their variability is outside of our scope. The following sections are instead devoted to a sensitivity study- a series of model integrations were employed to determine the necessary conditions for their generations. We will remark on possible sources of variability in our discussion.

Observations have determined that the mean mesoscale oceanic zonal velocity field is dominated by quasi-permanent jet-like features commonly referred to as striations (Maximenko et al., 2005; 2008; Huang et al., 2007; Ivanov et al., 2009; van Sebille et al., 2011; Buckingham and Cornillon, 2013). These features have also been detected in high-resolution ocean models (Nakano and Hasumi, 2005; Richards et al., 2006; Kamenkovich et al., 2009) including ROMS (Huang et al., 2007). Although mechanisms for the emergence of mean zonal jets have been suggested using theory and idealized models (Rhines 1975; Maltrud and Vallis 1991; Panetta 1993; Rhines, 1994; Cho and Polvani, 1996; Galperin et al., 2006; Nadiga, 2006; Baldwin et al., 2007; Dritschel and McIntyre, 2008), the dynamics underlying the formation of striations remain uncertain.

Scott et al. (2008) showed that mesoscale eddies follow preferred pathways as they propagate westward and so may produce the striated features seen in mean zonal velocity. Schlax and Chelton (2008) suggested that striations are an artifact of time-averaging extraordinarily large, yet still random mesoscale eddies. Melnichenko et al. (2010) showed, however, that eddies contribute to the potential vorticity (PV) variance of striations, indicating that they are dynamically distinct. Hristova et al. (2008) hypothesized that striations might be related to radiating instabilities of EBC's. Wang et al. (2012) showed using a simple single-layer quasi-geostrophic model that radiating modes excited nonlinearly within an EBC do indeed trigger striations.

Centurioni et al. (2008) reconstructed the time-mean map of geostrophic velocities at 15 m depth using drifters and satellite altimetry and found zonal currents connected to permanent meanders of the CCS. They proposed that vorticity associated with these meanders radiates Rossby waves that form stationary jets known as beta-plumes (Rhines, 1994; Afanasyev et al., 2012; Belmadani et al., 2013).

Here we test this hypothesis with sensitivity experiments using model output. By altering the model bathymetry, we remove the effect of topographic features and a continental slope. We then decrease the strength of atmospheric forcing by an order of magnitude to test the role of nonlinear dynamics, as well as coarsen the resolution of the model to 40 km to test the role of eddy variability. Finally, we replace the eastern boundary coastline with a flat meridional wall to test the effects of coastal geometry.

5.2: Sensitivity analysis with an ensemble of ROMS integrations

This analysis employs a set of 120-year ROMS integrations (Shchepetkin and McWilliams, 2005; Haidvogel et al., 2008, Curchitser et al., 2005) over 180°W-105°W; 9°N-53°N with a horizontal resolution of 20 km and 30 vertical layers. This configuration has captured both the mean and variability of the CCS (Marchesiello et al. 2003; Di Lorenzo et al., 2008; Di Lorenzo et al., 2009). Vertical diffusion is parameterized according to the Large/McWilliams/Doney scheme (Large et al., 1994). Forcing is a climatological NCEP wind stress (Kistler et al., 2001) without buoyancy fluxes. NCEP heat fluxes are employed with a nudging toward NOAA extended sea surface temperatures (SST's) (Smith and Reynolds, 2004) in order to avoid drifts in model SST (Josey, 2001). Horizontal boundaries are closed walls, and the control topography is extracted from Smith and Sandwell (1994). Integrations begin from rest with a uniform density profile extracted from the World Ocean Atlas 2005 (Locarnini et al., 2006; Antonov et al., 2006). Striations are diagnosed using zonal currents at 300 m, where the signature of the gyre circulation is reduced.

The role of topography is explored in a set of experiments (flat+slope) (Table 2), in which a uniform bottom depth (5000 m) is prescribed everywhere except along the eastern boundary (and around the Hawaiian and Aleutian islands). Here a uniform shelf slope was applied. The slope was taken from the average continental slope between 30°N and 40°N. Within the flat+slope set, the role of nonlinearity was determined by reducing the strength of the forcing by a factor of ten (flat+slope, weakly nonlinear). The role of mesoscale eddies was determined by further coarsening the grid to 40 km (flat+slope, weakly nonlinear, non-eddy resolving). In the flat runs, sensitivity to topography was determined by removing

the continental shelf and prescribing a uniform 5000 m bottom depth. In the wall run, the coastlines are replaced with a meridional wall at 125°W. The control, flat+slope, flat, and wall integrations are all able to reproduce the gyre circulation (Figures 25A-D).

Table 2 – ROMS integrations used in striation sensitivity experiments.

Exp. Name	Geometry	Forcing	Resolution
control	full topography (Fig. 1a)	full	20km
flat+slope	flat bottom at 5000m with uniform continental shelf along the eastern boundary (Fig. 1b)	full	20km
flat+slope, weakly non-linear		full*0.1	20km
flat+slope, weakly non-linear, non-eddy resolving		full*0.1	40km
flat	flat bottom at 5000m (Fig. 1c)	full	20km
flat, weakly non-linear		full*0.1	20km
flat, weakly non-linear, non-eddy resolving		full*0.1	40km
wall	flat bottom at 5000m with eastern boundary meridional wall (Fig. 1d)	full	20km
wall, weakly non-linear		full*0.1	20km
wall, weakly non-linear, non-eddy resolving		full*0.1	40km

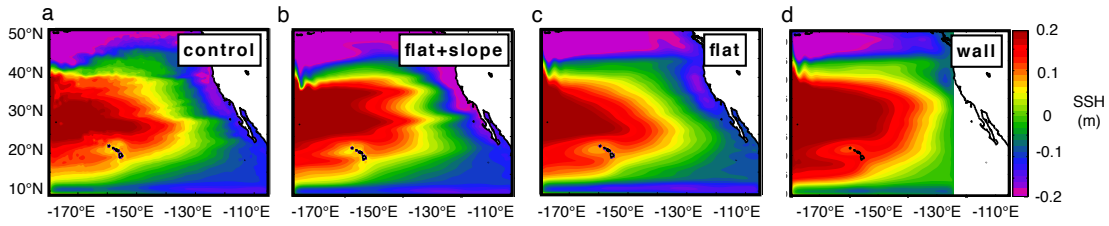

Figure 25 - (a-d) 120-year mean SSH (m) derived from the *control*, *flat +slope*, *flat*, and *wall* experiments, respectively (Table 2).

5.3: Striation formation across the ensemble

Progressive means of 300 m zonal velocities from the control run over the first 6, 12, and 120 months (Figures 26A-C) indicate that striations emerge as zonal plumes generated offshore from notable topographic features, as well as features of the California coastline, consistent with observations (Centurioni et al., 2008).

Progressive averages from the flat+slope experiment (using the idealized bathymetry and slope describes in Section 2) with full forcing and 20 km resolution (Figures 26D-F), show that, in the absence of topographic forcing, striations emerge on similar time scales and have similar magnitude, but evince more spatial coherence. This suggests that topography plays a significant, but lesser influence on offshore striations, in agreement with South Pacific observations (Buckingham and Cornillon 2013). It is, however, clear that the primary source of striation energy is located near the eastern boundary and that striation development is kinematically consistent with beta-plumes.

To determine the sensitivity of striation development to nonlinear background velocity regimes, we examine two additional flat+slope experiments, the first in which the magnitude of the wind forcing is reduced by a factor of ten (i.e. weakly nonlinear), and a second in which the resolution of the model is additionally coarsened to 40 km (i.e. weakly nonlinear and non-eddy-resolving). The results of these experiments are indistinguishable visually (not shown) and images are derived from the weakly nonlinear/eddy-resolving case (Figures 26G-I). Model output still evinces development of apparent eastern boundary beta-plumes. Striations still dominate 300 m zonal velocity and are maintained at a comparable magnitude to that of the full forcing case. Meanders take longer to develop with the

reduced wind energy input (Figure 26E,H), and striations are more strongly zonal due to a decreased large-scale circulation.

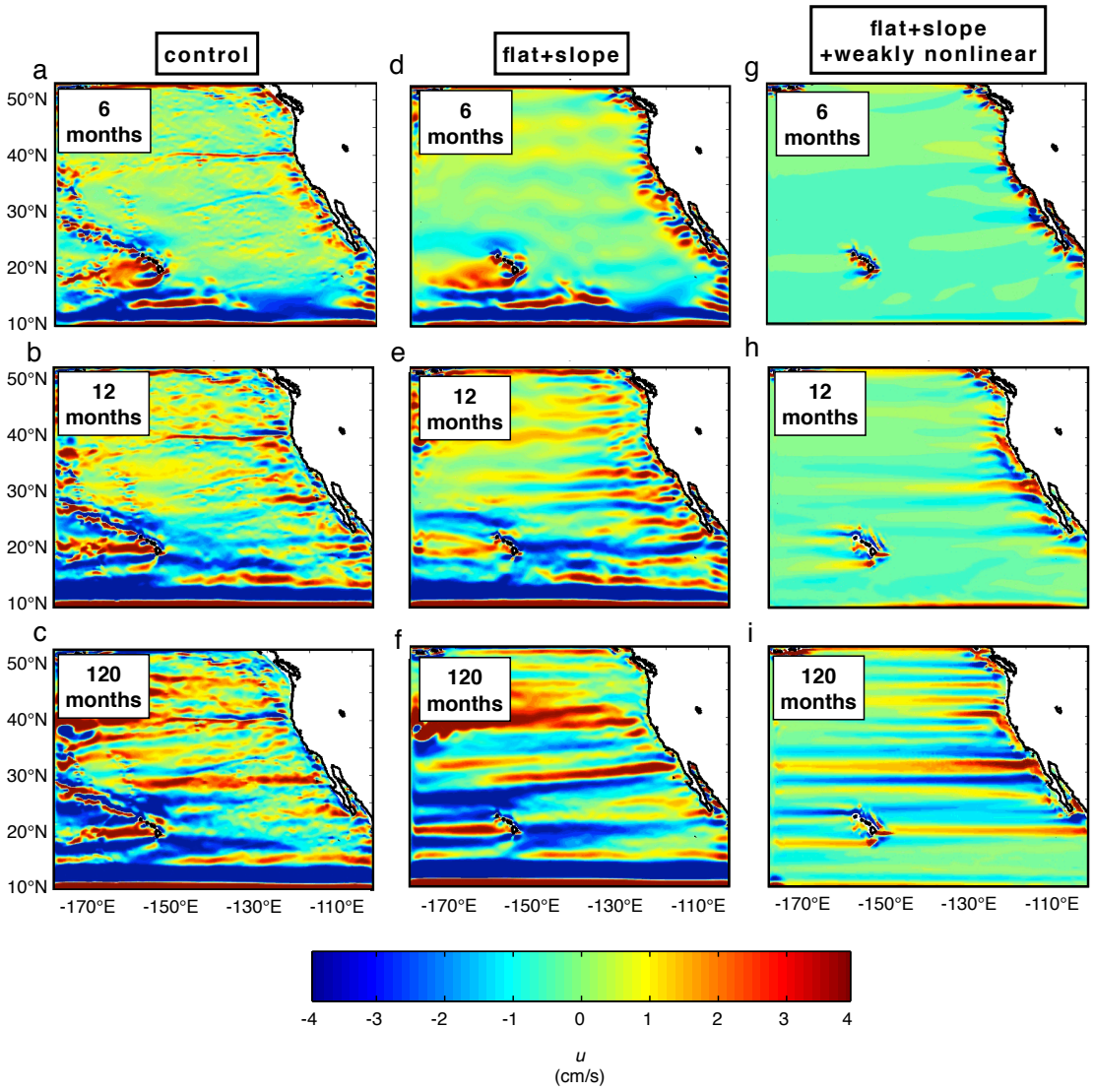

Figure 26 - (a-c) Zonal currents at 300 m depth (cm s-1) averaged over the first 6, 12, and 120 months, respectively, from the *control* experiment. (d-f) and (g-i) same as (a-c) for the *flat+slope* experiment and *flat+slope* weakly nonlinear experiment (Table 2), respectively.

To evaluate the importance of the continental slope in the formation of striations, we performed three experiments with uniform 5000 m bottom depth and vertical continental boundaries (flat experiments, Table 2). When we remove the continental sole in the flat experiment, the magnitude of striations decreases to roughly half that of the control and flat+slope runs (Figures 27A-C) even though the wind forcing is the same, and the gyre circulation is maintained at the same magnitude (Figures 25B,C). The meanders that are sources of vorticity for striations are weaker in the flat run (Figure 25C), which may explain the reduced striation magnitude. Continental slopes also impose a dynamical boundary to the offshore propagation of potential vorticity anomalies, so that anomalies from the coast are "trapped" on the shelf and unable to propagate freely offshore until they reach a critical magnitude. Although we do not examine the dynamics of this potential vorticity trapping in detail, we hypothesize that the absence of the continental slope in the flat run allows beta plumes to propagate westward independently of their magnitude. Consistent with this hypothesis, when we reduce the wind magnitude by a factor of ten in the flat weakly nonlinear experiment (Table 2), striation strength is also reduced by an order of magnitude (Figures 27D-F). This linear response to the wind magnitude is not observed in the flat+slope case, where reducing the wind forcing by an order of magnitude only reduces striation strength by a small fraction (Figures 26F,I). This leads us to conclude that without a continental slope, striations freely propagate offshore as they develop, whereas in the slope case, anomalies must reach a critical magnitude in order to escape. Despite the slower spin-up of the CCS in the weakly nonlinear flat+slope experiment, the magnitude enforced by the slope ensures that striations remain strong in the mean (Figure

26I). The results of the flat weakly nonlinear non-eddy-resolving experiments are again visually indistinguishable and are not presented.

The role of coastal geometry was further explored in the wall experiments (Table 2) by removing the coastline and setting a wall along the eastern boundary (125°W) (Figure 25D). While the spin-up is characterized by the formation of striations, they are short-lived in the mean, and their signature eventually disappears (Figures 27G-I). Striations are subsumed in the mean because meanders are no longer anchored to coastal features and propagate freely, consistent with the Wang et al. (2012) model.

These results strongly suggest that the strongest NEP striations arise from the coast, as their magnitude remained constant within the *flat* runs. They are also almost certainly anchored by features of the coastline, as they are not apparent in the long-term integrations of the *wall* grid. They are also distinct from eddies, given that they form in thoroughly linear flow regimes and eddy-precluding resolutions. This supports our initial hypothesis-that striations represent the westward migration of persistent CCS vorticity sources as beta-plumes.

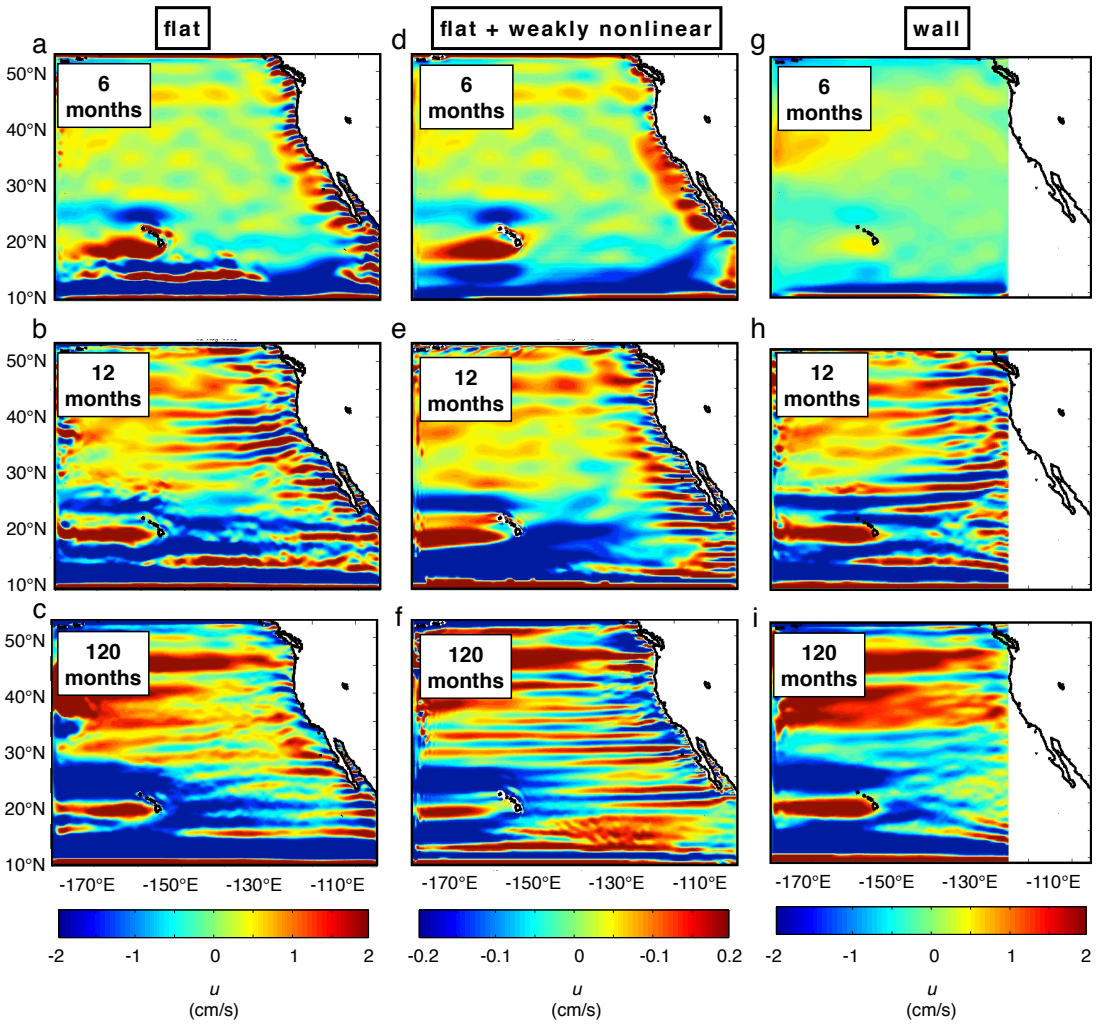

Figure 27 - (a-c) Same as Fig. 26, except from the *flat* experiment. (d-f) and (g-i) same as (a-c) for the *flat* weakly nonlinear and *wall* experiments (Table 1), respectively. (see text). Note the difference in color scales between Figures 2 and 3, as well as between 27d-f and 27a-c.

Chapter 6: Conclusion and discussion

This work has examined the nature of three distinct means of CCS transport- large-scale meridional currents, mesoscale eddies, and striations. While in all cases ROMS output was used to effectively recreate these phenomena, because of the differing spatial and temporal scales involved, sometimes disparate methods of analysis were employed. This necessitates discussion that treats with each topic in turn.

In section 3, we asked by what method large-scale transports in the CCS were most effectively forced. This we couched as a competition between two hypotheses- each proposing an alternate dominant forcing mechanism. The first hypothesis maintains that mean alongshore transports are dominated by CTW variance, which radiates offshore as long Rossby waves. The associated SSHa gradients then produce anomalous geostrophic alongshore currents that control large-scale variance (Figure 3A). The second hypothesis asserts that the local cross-shelf stationary gradient in wind stress curl anomalies alter the large-scale stationary SSH gradient through Ekman pumping (Figure 3B).

The CTW and WSC hypotheses were tested using the OBC1 and no OBC ROMS hindcasts for the period 1950-2008. Analysis of the correlation between model output SSHa and Niño 3.4 (Figure 5A—D), as well as the effective propagation of coastal SSHa as Rossby waves (Figure 7B,D; Figure 13) indicated that the mechanisms of large-scale SSHa are consistent with the CTW hypothesis. However, CCS alongshore currents did not show meaningful offshore propagation (Figure 8B,D; Figure 14), or any tropical influence (Figure 5E—L) and were inconsistent with this framework.

The failure of the CTW hypothesis in hindcasting CCS meridional current variability led us to explore the role of local wind forcing as the primary driver of meridional transport variability. We quantified the fraction of deterministic variance associated with wind stress by developing a single index of mean alongshore transports in both ROMS integrations, irrespective of the inclusion of CTW's of tropical origin (Figure 9). These indices track the time variability of the core of the CC equatorward flow. The correlation between the two raw monthly indices was significant (R=0.7) and explained a large fraction of the total variance (40%-50%) indicating that most of the signal was forced locally. The role of the local forcing was further diagnosed by extracting the patterns of wind stress curl that drive the meridional transport indices. We found that a spatially stationary wind stress curl pattern with a cross-shelf gradient accounted for the largest fraction of variance in stationary SSH gradients as well as transport indices (Figure 11B) in accordance with the dynamical theory presented in section 1. This wind pattern is the dominant mode of local wind variability, and represents a strengthening and weakening of the mean wind stress curl cross-shelf gradient (Figure 11).

The effectiveness of this wind stress curl pattern in hindcasting our transport index leads us to a revised system of CCS alongshore current variability. Whereas SSHa variance is concentrated on large spatial scales (>200km), v_e is dominated by mesoscale variability (Figure 15E,F). It is, however, energized by an offshore wind stress curl gradient, which is ultimately responsible for much of the driven large-scale (>200km) transport variability.

While the CTW mechanism fails to effectively hindcast v_e, it does account for a large amount of SSHa variability. This contrast is most likely due to the large-scale Rossby waves radiated by CTW's. On monthly time scales and longer,

the magnitude of velocity anomalies should be prescribed by geostrophic balance. The small wavenumber associated with these large-scale Rossby waves means that the associated gradients (and *v* anomalies) are small in comparison to the scale of mean flow. If we describe the SSH anomalies associated with large-scale Rossby waves as

$$SSHa = Ae^{ik(x-ct)} \tag{12}$$

where A is an arbitrary constant, then the corresponding *v* anomalies will be

$$v_a = \frac{Akg}{f} e^{ik(x-ct)} \tag{13}$$

.

As the waves grow longer and *k* decreases, the *v* anomalies grow smaller as well. If, as we saw, CCS currents are best characterized by meanders and are dominated by mesoscale variance, these anomalies will have little impact on mean flow. Large-scale *v* anomalies are stationary, and attached to similarly stationary SSH variability. Although we made no distinction in the analysis between free tropical CTW's and semi-local wind-forced CTW's, the lack of effective propagation of transport anomalies as long Rossby waves (Figure 8B,E) strongly suggest that neither plays a significant role in offshore flow patterns.

Large-scale transports are instead forced by a specific local pattern of wind variability. However, not all the variance of the wind local forcing is independent of ENSO and the large-scale climate. The ENSO teleconnections on the Aleutian Low that drive an ocean response in the PDO pattern project also on the local wind stress

curl pattern, and a significant fraction (R=0.4) of meridional transport variability is captured by the PDO (Figure 13A). This implies that low-frequency modulations of the meridional flow are also sensitive to larger Pacific climate modes through atmospheric teleconnections.

Given the large amount of transport variance concentrated on the mesoscale (Figure 15F), our next task was to quantify mesoscale eddy variability, as well as determine by what (if anything), it was effectively forced. Our results are strong evidence that in the NCC, local wind variability regulates mesoscale eddy activity on interannual and decadal time scales, just as it does seasonally. While there remains a significant amount of intrinsic variance on these time scales, the deterministic component is composed of both barotropic and baroclinic variability in the large-scale flow, both of which are modulated by wind stress curl gradients. This is in accord with the analysis of large-scale transports, which were also driven by an cross-shelf wind stress curl gradient. In the SCC, there is very little forced variance in evidence. The recirculation and attendant feedbacks add noise and intrinsic variability which dominate any deterministic component.

In section 3, we showed that the influence of coastal trapped waves on large-scale SSHa and alongshore currents diminished north of the Southern California Bight. It was largely for this reason that we split our two areas of study along this latitude. We investigated the possibility that ENSO impacts mesoscale eddy activity in the SCC (as reported by Keister and Strub (2008)), and results were mixed. SCC anticyclone and cyclone counts coming from our “OBC1” model run showed weakly significant negative correlations with Niño 3.4 at a lag of 6 months. Eddy counts from the “no OBC” run were uncorrelated with Niño 3.4 (as expected, given its time-independent boundary condition) but those from “OBC 2”

were, as well. With only one of the two OBC runs evincing an ENSO signal in eddy counts, we can only say that there is conflicting evidence of tropical influence on CCS mesoscale activity.

It should be noted that although our three model simulations employed in the analysis of large-scale transports and mesoscale eddies could reproduce the stationary statistics and broad spatial patterns of the CCS, there are some inconsistencies in the hindcast. Large-scale transports were authenticated in previous publications (Di Lorenzo et al. 2008; 2009), but here we compared model eddy activity to that derived from AVISO altimetry. While the hindcasts did reproduce the broad spatial patterns, seasonal cycle, and some interannual variability there is ample cause to suspect dissimilarity with actual eddy activity. Modeled NCC eddies propagate offshore further north than in observations, and modeled SCC eddies propagate less effectively. This may add artificial intrinsic variance to modeled SCC eddy counts. AVISO itself may not resolve some nearshore mesoscale activity, limiting the scope of model validation. In addition, the coarse NCEP reanalysis winds used to force our model cannot resolve fine-scale wind variability, which may also play a role in eddy formation.

In addition to its resolution, NCEP II reanalysis has a number of biases in its mean spatial structure, especially around the CCS. While we maintain that this does not undercut the analysis, (largely because of the ability of our integrations to capture the interannual variability of both large-scale flow and NCC mesoscale activity), it does introduce some additional magnitude to the mean curl pattern.

As well as caveats concerning the agreement of our model with observations, there are several limitations inherent in the largely theoretical approach taken here. Although our barotropic and baroclinic indices were based

on mechanisms widely theorized to underly eddy formation, we have not attempted to describe the process in detail. A full dynamical approach to this question could establish precisely how wind stress curl anomalies contribute variance to instability along both these pathways. We leave this to future studies.

The treatment of mesoscale activity as a forced, rather than coupled, process is also inherently limiting, especially in our study of the SCC. The relatively simple correlation analysis used here is not suited to the strongly nonlinear nature of SCC eddy processes. A more sophisticated modeling approach is needed if the interplay of atmospheric forcing, CTW forcing, large-scale flow, and mesoscale activity is to be effectively diagnosed.

In addition to the variability of alongshore and eddy transports, we also examined the formation of semi-permanent zonal currents known as striations. By analyzing the spin-up of our series of ROMS integrations, we showed that Northeast Pacific striations are not necessarily forced by surface fluxes of momentum or buoyancy, but can develop from vorticity sources associated with topography and/or instabilities along the eastern boundary, a process for which we propose the following mechanism.

EBC flow is unstable (Walker and Pedlosky 2002, Hristova et al. 2008, Wang et al. 2012), and generates meanders that are anchored to coastal features (Batteen, 1997; Centurioni et al., 2008). The associated vorticity propagates westward as a beta-plume, consistent with observations of striation attachment to CCS meanders (Centurioni et al. 2008). It also agrees with the two most basic observations presented here: that persistent striations are energized within the boundary current as it spins up, and that they develop primarily in response to coastal geometry. This progression is most clear in the *flat* experiment (Figures

27A-C,), where jet patterns remain in the absence of bottom topography and continental slope, and in the *wall* experiment, in which permanent striations could not develop without coastal features to anchor vorticity anomalies.

These results strongly suggest that intense striations arise at the coast. The fact that striations emerge in a non-eddying regime indicates that they are unlikely to result solely from time-averaged mesoscale eddy tracks, consistently with recent results from idealized models (Nadiga and Straub, 2010) and observations (Ivanov et al., 2012; Buckingham and Cornillon, 2013). The extreme contrast in magnitude between the *flat+slope* weakly nonlinear and *flat* weakly nonlinear experiments indicates that potential vorticity trapping constrains striation strength.

There are a number of significant idealizations in our model runs. Climatological wind forcing precludes small-scale winds that may modulate striations (Chelton et al., 2004; Taguchi et al., 2012). NCEP winds also produce biases in EBC's (Colas et al., 2012; Cambon et al., 2013), which may alter stratification and associated coastal instabilities. A purely kinematic treatment is also limited in its ability to determine the wider role of striations in the mean circulation, as well as to generalize to other basins. Further study that focuses on the dynamics and vorticity budgets of striations will be vital an understanding of the dynamical balances associated with their generation.

REFERENCES

Afanasyev, Y. D., O'Leary, S., Rhines, P. B., Lindahl, E., 2012. On the origin of jets in the ocean, Geophys. Astrophys. Fluid Dyn. 106(2), 113-137.

Alexander, M. A., 1992. Midlatitude atmosphere ocean interaction during el nino .2. The Northern-hemisphere atmosphere. Journal of Climate 5, 959-972.

Alexander, M. A., Blade, I., Newman, M., Lanzante, J. R., Lau, N. C., Scott, J. D., 2002. The atmospheric bridge: The influence of ENSO teleconnections on air-sea interaction over the global oceans. Journal of Climate 15, 2205-2231.

Antonov, J. I., Locarnini, R. A., Boyer, T. P., Mishonov, A. V., Garcia, H. E., 2006. World Ocean Atlas 2005, Volume 2: Salinity. S. Levitus, Ed. NOAA Atlas NESDIS 62, U.S. Government Printing Office, Washington, D.C., 182 pp.

Baldwin, M. P., Rhines, P. B., Huang, H. P., McIntyre, M. E., 2007. The jet-stream conundrum. Science 315, 467-468.

Barth, J. A., Pierce, S. D., Smith, R. L., 2000. A separating coastal upwelling jet at Cape Blanco, Oregon and its connection to the California Current System. Deep-Sea Research II 47, 783-810.

Batteen, M. L., 1997. Wind-forced modeling studies of currents, meanders, and eddies in the California Current system. Journal of Geophysical Research-Oceans, 102, 985-1010.

Battisti, D. S., Hickey, B. M., 1984. Application of remote wind-forced coastal trapped wave theory to the Oregon and Washington coasts. Journal of Physical Oceanography 14, 887-903.

Belmadani, A., Maximenko, N. A., McCreary, J. P., Furue, R., Melnichenko, O. V., Schneider, N., Di Lorenzo, E., 2013. Linear wind-forced beta plumes with application to the Hawaiian Lee Countercurrent, J. Phys. Oceanogr., doi:10.1175/JPO-D-12-0194.1

Bograd, S. J., Lynn, R. J., 2003. Long-term variability in the Southern California Current System. Deep-Sea Research Part Ii-Topical Studies in Oceanography 50, 2355-2370 .

Brink, K. H., Beardsley, R. C., Paduan, J., Limeburner, R., Caruso, M., Sires, J. G., 2000. A view of the 1993-1994 California Current based on surface drifters, floats, and remotely sensed data. Journal of Geophysical Research-Oceans 105, 8575-8604.

Buckingham, C. E., Cornillon, P. C., 2013. The contribution of eddies to striations in absolute dynamic topography. Journal of Geophysical Research-Oceans, 118, 448-461.

Cambon, G., Goubanova, K., Marchesiello, P., Dewitte, B., Illig, S., Echevin, V., 2013. Assessing the impact of downscaled winds on a regional ocean model simulation of the Humboldt system. Ocean Modelling, 65, 11-24.

Cane, M. A., Moore, D. W., 1981. A note on low-frequency equatorial basin modes. Journal of Physical Oceanography 11, 1578-1584.

Centurioni, L. R., Ohlmann, J. C., Niiler, P. P., 2008. Permanent meanders in the California Current System. Journal of Physical Oceanography, 38, 1690-1710.

Chaigneau, A., Eldin, G., Dewitte, B., 2009. Eddy activity in the four major upwelling systems from satellite altimetry (1992-2007). Progress in Oceanography 83, 117-123.

Chaigneau, A., Gizolme, A., Grados, C., 2008. Mesoscale eddies off Peru in altimeter records: Identification algorithms and eddy spatio-temporal patterns. Progress in Oceanography 79, 106-119.

Chelton, D. B., Davis, R. E., 1982. Monthly mean sea-level variability along the west coast of North America. Journal of Physical Oceanography 12, 757-784.

Chelton, D. B., Schlax, M. G., Freilich, M. H., Milliff, R. F., 2004. Satellite measurements reveal persistent small-scale features in ocean winds. Science, 303, 978-983.

Chelton, D. B., Schlax, M. G., Samelson, R. M., 2011. Global observations of nonlinear mesoscale eddies. Progress in Oceanography 91, 167-216.

Chelton, D. B., Schlax, M. G., Samelson, R. M., de Szoeke, R. A., 2007. Global observations of large oceanic eddies. Geophysical Research Letters 34, L15606, doi: 10.1029/2007gl030812.

Chereskin, T. K., Morris, M. Y., Niiler, P. P., Kosro, P. M., Smith, R. L., Ramp, S. R., Collins, C. A., Musgrave, D. L., 2000. Spatial and temporal characteristics of the mesoscale circulation of the California Current from eddy-resolving moored and shipboard measurements. Journal of Geophysical Research-Oceans 105,1245-1269.

Cho, J. Y. K., Polvani, L. M., 1996. The emergence of jets and vortices in freely evolving, shallow-water turbulence on a sphere. Physics of Fluids, 8, 1531-1552.

Clarke, A. J., Dottori, M., 2008. Planetary wave propagation off california and its effect on Zooplankton. Journal of Physical Oceanography 38, 702-714.

Clarke, A. J., Shi, C., 1991. Critical frequencies at ocean boundaries. Journal of Geophysical Research-Oceans. Journal of Geophysical Research-Oceans 96, 10731-10738.

Colas, F., McWilliams, J. C., Capet, X., Kurian, J., 2012. Heat balance and eddies in the Peru-Chile current system. Clim. Dyn., 39, 509-529.

Combes, V., Chenillat, F., Di Lorenzo, E., Riviere, P., Ohman, M. D., Bograd, S. J., 2013. Cross-shore transport variability in the California Current: Ekman upwelling vs. eddy dynamics. Progress in Oceanography 109, 78-89.

Cornuelle, B. D., Chereskin, T. K., Niiler, P. P., Morris, M. Y., Musgrave, D. L., 2000. Observations and modeling of a California undercurrent eddy. Journal of Geophysical Research-Oceans 105, 1227-1243.

Curchitser, E. N., Haidvogel, D. B., Hermann, A. J., Dobbins, E. L., Powell, T. M., Kaplan, A., 2005. Multi-scale modeling of the North Pacific Ocean: Assessment and analysis of simulated basin-scale variability (1996-2003). Journal of Geophysical Research-Oceans, 110.

Di Lorenzo, E., et al., 2009. Nutrient and salinity decadal variations in the central and eastern North Pacific. Geophysical Research Letters 36, L14601, doi: 10.1029/2009gl038261.

Di Lorenzo, E., et al., 2008. North Pacific Gyre Oscillation links ocean climate and ecosystem change. Geophysical Research Letters 35, L08607, doi: 10.1029/2007gl032838.

Di Lorenzo, E., Schneider, N., Cobb, K. M., Franks, P. J. S., Chhak, K., Miller, A. J., McWilliams, J. C., Bograd, S. J., Arango, H., Curchitser, E., Powell, T. M., Riviere, P., 2008 North Pacific Gyre Oscillation links ocean climate and ecosystem change. Geophys. Res. Lett., 35, L08607, doi:10.1029/2007GL032838.

Dorr, A., Grimshaw, R., 1986. Barotropic continental-shelf waves on a beta-plane. Journal of Physical Oceanography 16, 1345-1358.

Dritschel, D. G., McIntyre, M. E., 2008. Multiple jets as PV staircases: The Phillips effect and the resilience of eddy-transport barriers. Journal of the Atmospheric Sciences, 65, 855-874.

Enfield, D. B., Allen, J. S., 1980. On the structure and dynamics of monthly mean seas-level anomalies along the pacific coast of North and South America. Journal of Physical Oceanography 10, 557-578.

Enfield, D. B., Allen, J. S., 1983. The generation and propagation of sea-level variability along the Pacific coast of Mexico. Journal of Physical Oceanography 13, 1012-1033.

Fu, L. L., Qiu, B., 2002. Low-frequency variability of the North Pacific Ocean: The roles of boundary- and wind-driven baroclinic Rossby waves. Journal of Geophysical Research-Oceans 107, 3220, doi: 10.1029/2001jc001131.

Fukumori, I., Lee, T., Cheng, B., Menemenlis, D., 2004. The origin, pathway, and destination of Nino-3 water estimated by a simulated passive tracer and its adjoint. Journal of Physical Oceanography 34, 582-604.

Galperin, B., Sukoriansky, S., Dikovskaya, N., Read, P. L., Yamazaki, Y. H., and Wordsworth, R., 2006. Anisotropic turbulence and zonal jets in rotating flows with a beta-effect, Nonlinear Processes in Geophysics, 13(1), 83-98.

Gill, A. E., 1982. Atmosphere-Ocean Dynamics. Academic Press, New York 662 pp.

Grimshaw, R., Allen, J. S., 1988. Low-frequency baroclinic waves off coastal boundaries. Journal of Physical Oceanography 18, 1124-1143.

Gruber, N., Frenzel, H., Doney, S. C., Marchesiello, P., McWilliams, J. C., Moisan, J. R., Oram, J. J., Plattner, G. K., Stolzenbach, K. D., 2006. Eddy-resolving simulation of plankton ecosystem dynamics in the California Current System. Deep-Sea Research I 53, 1483-1516.

Gruber, N., Lachkar, Z., Frenzel, H., Marchesiello, P., Munnich, M., McWilliams, J. C., Nagai, T., Plattner, G. K., 2011. Eddy-induced reduction of biological production in eastern boundary upwelling systems. Nature Geoscience 4, 787-792.

Haidvogel, D. B., et al., 2008. Ocean forecasting in terrain-following coordinates: Formulation and skill assessment of the Regional Ocean Modeling System. Journal of Computational Physics 227, 3595-3624.

Hermann, A. J., Curchitser, E. N., Haidvogel, D. B., Dobbins, E. L., 2009. A comparison of remote vs. local influence of El Nino on the coastal circulation of the northeast Pacific. Deep-Sea Research Part II-Topical Studies in Oceanography 56, 2427-2443.

Hickey, B. M., 1984. The fluctuating longshore pressure-gradient on the Pacific Northwest shelf - A dynamical analysis. Journal of Physical Oceanography 14, 276-293.

Hickey, B. M., 1998. Coastal Oceanography of Western North America from the tip of Baja California to Vancouver Island, in: Robinson, A. R., Brink, K. H. (Eds.), The Sea. John Wiley & Sons, New York, pp. 345-391.

Hickey, B. M., Banas, N. S., 2003. Oceanography of the US Pacific Northwest Coastal Ocean and estuaries with application to coastal ecology. Estuaries 26, 1010-.

Hristova, H. G., Pedlosky, J., Spall, M. A., 2008. Radiating instability of a meridional boundary current. Journal of Physical Oceanography, 38, 2294-2307.

Isern-Fontanet, J., Garcia-Ladona, E., Font, J., 2003. Identification of marine eddies from altimetric maps. Journal of Atmospheric and Oceanic Technology 20, 772-778.

Ivanov, L. M., Collins, C. A., Margolina, T. M., 2009. System of quasi-zonal jets off California revealed from satellite altimetry, Geophysical Research Letters, 36.

Ivanov, L. M., Collins, C. A., Margolina, T. M., 2012. Detection of oceanic quasi-zonal jets from altimetry observations, J. Atmos. Ocean. Technol., 29, 1111-1126, doi:10.1175/JTECH-D-11-00130.1.

Jeronimo, G., Gomez-Valdes, J., 2007. A subsurface warm-eddy off northern Baja California in July 2004. Geophysical Research Letters 34, L06610, doi: 10.1029/2006gl028851.

Josey, S. A., 2001. A comparison of ECMWF, NCEP-NCAR, and SOC surface heat fluxes with moored buoy measurements in the subduction region of the Northeast Atlantic. Journal of Climate, 14, 1780-1789.

Kalnay, E., et al., 1996. The NCEP/NCAR 40-year reanalysis project. Bulletin of the American Meteorological Society 77, 437-471.

Kamenkovich, I., P. Berloff, and J. Pedlosky, 2009: Anisotropic Material Transport by Eddies and Eddy-Driven Currents in a Model of the North Atlantic. Journal of Physical Oceanography, 39, 3162-3175.

Keister, J. E., Strub, P. T., 2008. Spatial and interannual variability in mesoscale circulation in the northern California Current System. Journal of Geophysical Research-Oceans 113, C04015, doi: 10.1029/2007jc004256.

Kelly, K. A., Beardsley, R. C., Limeburner, R., Brink, K. H., Paduan, J. D., Chereskin, T. K., 1998. Variability of the near-surface eddy kinetic energy in the California Current based on altimetric, drifter, and moored current data. Journal of Geophysical Research-Oceans 103, 13067-13083.

Killworth, P. D., Chelton, D. B., DeSzoeke, R. A., 1997. The speed of observed and theoretical long extratropical planetary waves. Journal of Physical Oceanography 27, 1946-1966.

Kistler, R., and Coauthors, 2001. The NCEP-NCAR 50-year reanalysis: Monthly means CD-ROM and documentation. Bulletin of the American Meteorological Society, 82, 247-267.

Kurczyn, J. A., Beier, E., Lavin, M. F., Chaigneau, A., 2012. Mesoscale eddies in the northeastern Pacific tropical-subtropical transition zone: Statistical characterization from satellite altimetry. Journal of Geophysical Research-Oceans 117, C10021, doi: 10.1029/2012jc007970.

Kurian, J., Colas, F., Capet, X., McWilliams, J. C., Chelton, D. B., 2011. Eddy properties in the California Current System. Journal of Geophysical Research-Oceans 116, C08027, doi: 10.1029/2010jc006895

Large, W. G., McWilliams, J. C., Doney, S. C., 1994. Oceanic Vertical Mixing - A Review and a Model with a Nonlocal Boundary-layer Parameterization. Reviews of Geophysics, 32, 363-403.

Locarnini, R. A., Mishonov, A. V., Antonov, J. I., Boyer, T. P., Garcia, H. E., 2006. World Ocean Atlas 2005, Volume 1: Temperature. S. Levitus, Ed. NOAA Atlas NESDIS 61, U.S. Government Printing Office, Washington, D.C., 182 pp.

Maltrud, M. E., Vallis, G. K., 1991. Energy-spectra and Coherent Structures in Forced 2-dimensional and Beta-plane Turbulence. Journal of Fluid Mechanics, 228, 321-&.

Mantua, N. J., Hare, S. R., Zhang, Y., Wallace, J. M., Francis, R. C., 1997. A Pacific interdecadal climate oscillation with impacts on salmon production. Bulletin of the American Meteorological Society 78, 1069-1079.

Marchesiello, P., McWilliams, J. C., Shchepetkin, A., 2001. Open boundary conditions for long-term integration of regional oceanic models. Ocean Modelling 3, 1-20.

Marchesiello, P., McWilliams, J. C., Shchepetkin, A., 2003. Equilibrium structure and dynamics of the California Current System. Journal of Physical Oceanography 33, 753-783.

Masumoto, Y., and Coauthors, 2004. A fifty-year eddy-resolving simulation of the World Ocean—Preliminary outcomes of OFES (OGCM for the Earth Simulator). J. Earth Simul 1, 35-36.

Maximenko, N. A., Bang, B., Sasaki, H., 2005. Observational evidence of alternating zonal jets in the world ocean, Geophysical Research Letters, 32(12).

Maximenko, N. A., Melnichenko, O. V., Niiler, P. P., Sasaki, H., 2008. Stationary mesoscale jet-like features in the ocean, Geophysical Research Letters, 35(8).

McGillicuddy, D. J., et al., 2007. Eddy/wind interactions stimulate extraordinary mid-ocean plankton blooms. Science 316, 1021-1026.

Melnichenko, O. V., Maximenko, N. A., Schneider, N., Sasaki, H. (2010), Quasi-stationary striations in basin-scale oceanic circulation: vorticity balance from observations and eddy-resolving model, Ocean Dynamics, 60(3), 653-666.

Mooers, C. N. K., Smith, R. L., 1968. Continental shelf waves off Oregon. Journal of Geophysical Research 73, 549-557.

Nadiga, B. T., 2006. On zonal jets in oceans. Geophysical Research Letters, 33.

Nadiga, B. T., Straub, D. N., 2010. Alternating zonal jets and energy fluxes in barotropic wind-driven gyres, Ocean Modelling, 33(3-4), 257-269.

Nakano, H., Hasumi, H., 2005. A series of zonal jets embedded in the broad zonal flows in the pacific obtained in eddy-permitting ocean general circulation models. Journal of Physical Oceanography, 35, 474-488.

Niiler, P. P., Maximenko, N. A., McWilliams, J. C., 2003. Dynamically balanced absolute sea level of the global ocean derived from near-surface velocity observations. Geophysical Research Letters 30, 2164, doi: 10.1029/2003gl018628..

Okubo, A., 1970. Horizontal dispersion of floatable particles in vicinity of velocity singularities such as convergences. Deep-Sea Research 17, 445-454.

Panetta, R. L., 1993. Zonal Jets in Wide Baroclinically Unstable Regions - Persistence and Scale Selection. Journal of the Atmospheric Sciences, 50, 2073-2106.

Paressierra, A., White, W. B., Tai, C. K., 1993. Wind-driven coastal generation of annual mesoscale eddy activity in the California Current. Journal of Physical Oceanography 23, 1110-1121.

Peltier, W. R., Stuhne, G., 2002. The upscale turbulence cascade: shear layers, cyclones and gas giant bands. Meteorology at the Milennium. R. P. Pearce, Ed., Academic Press. 43-61.

Rhines, P. B., 1975. Waves and Turbulence on a Beta-plane. Journal of Fluid Mechanics, 69, 417-443.

——, 1994: Jets. Chaos, 4, 313-339.

Richards, K. J., Maximenko, N. A., Bryan, F. O., Sasaki, H. 2006. Zonal jets in the Pacific Ocean, Geophysical Research Letters, 33(3).

Schlax, M. G., Chelton, D. B., 2008. The influence of mesoscale eddies on the detection of quasi-zonal jets in the ocean, Geophysical Research Letters, 35(24).

Schopf, P. S., Anderson, D. L. T., Smith, R., 1981. Beta dispersion of low-frequency Rossby Waves. Dynamics of Atmospheres and Oceans 5, 187-214.

Shchepetkin, A. F., McWilliams, J. C., 2003. A method for computing horizontal pressure-gradient force in an oceanic model with a nonaligned vertical coordinate. Journal of Geophysical Research-Oceans 108, 3090, doi: 10.1029/2001jc001047.

Shchepetkin, A. F., McWilliams, J. C., 2005. The regional oceanic modeling system (ROMS): a split-explicit, free-surface, topography-following-coordinate oceanic model. Ocean Modelling, 9, 347-404.

Smith, T. M., Reynolds, R. W., 2004. Improved extended reconstruction of SST (1854-1997). Journal of Climate, 17, 2466-2477.

Smith, W. H. F., Sandwell, D. T., 1994, Bathymetric Prediction from Dense Satellite Altimetry and Sparse Shipboard Bathymetry. Journal of Geophysical Research-Solid Earth, 99, 21803-21824.

Stegmann, P. M., Schwing, F., 2007. Demographics of mesoscale eddies in the California Current. Geophysical Research Letters 34, L14602, doi: 10.1029/2007gl029504.

Strub, P. T., James, C., 2000. Altimeter-derived variability of surface velocities in the California Current System: 2. Seasonal circulation and eddy statistics. Deep-Sea Research II 47, 831-870.

Taguchi, B., Furue, R., Komori, N., Kuwano-Yoshida, A., Nonaka, M., Sasaki, H., Ohfuchi, W., 2012. Deep oceanic zonal jets constrained by fine-scale wind stress curls in

the South Pacific Ocean: A high-resolution coupled GCM study. Geophysical Research Letters, 39. L08602, doi: 10.1029/2012GL051248

van Sebille, E., Kamenkovich, I,Willis, J. K., 2011. Quasi-zonal jets in 3-D Argo data of the northeast Atlantic. Geophysical Research Letters, 38.

Walker, A., Pedlosky, J., 2002 Instability of meridional baroclinic currents. Journal of Physical Oceanography, 32, 1075-1093.

Wang, J., Spall, M. A., Flierl, G. R., Malanotte-Rizzoli, P., 2012. A new mechanism for the generation of quasi-zonal jets in the ocean, - Geophysical Research Letters, 39, L10601, doi: 10.1029/2012GL051861

Weiss, J., 1991. The dynamics of enstrophy transfer in 2-dimensional hydrodynamics. Physica D 48, 273-294.